

AD-A113 534

SCIENTIFIC RESEARCH ASSOCIATES INC GLASTONBURY CT

F/6 20/4

COMPUTATION OF TURBULENT HORSESHOE VORTEX FLOW PAST SWEEP AND U-ETC(U)

MAR 82 W R BRILEY, H MCDONALD

N00014-77-C-0075

UNCLASSIFIED

SRA-R82-920001-F

NL

1 OF 1
AD-A
134 13

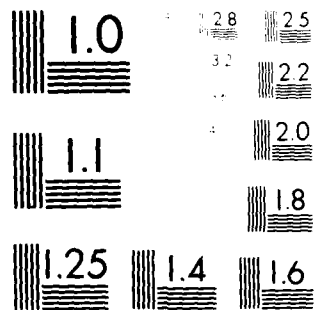
END

DATE

FILED

15-82

DTIC



Minimum Resolvable Pattern Element
Resolution Test Chart

(12)

Report R82-920001-F

COMPUTATION OF TURBULENT HORSESHOE VORTEX FLOW
PAST SWEEPED AND UNSWEEPED LEADING EDGES

W. R. Briley and H. McDonald
Scientific Research Associates, Inc.
P.O. Box 498
Glastonbury, CT 06033

March 1982

Final Report for Period 1 January 1980 - 31 December 1981

Approved for Public Release; Distribution Unlimited

Prepared for:

OFFICE OF NAVAL RESEARCH
800 N. Quincy Street
Arlington, VA 22217

DTIC
ELECTE
APR 13 1982
B

82 04 12 126

AD A113534

DTIC FILE COPY

REPORT DOCUMENTATION PAGE		READ INSTRUCTIONS BEFORE COMPLETING FORM
1. REPORT NUMBER R82-920001-F	2. GOVT ACCESSION NO. AD A113534	3. RECIPIENT'S CATALOG NUMBER
4. TITLE (and Subtitle) Computation of Turbulent Horseshoe Vortex Flow Past Swept and Unswept Leading Edges		5. TYPE OF REPORT & PERIOD COVERED Final Report 1 Jan. 80 to 31 Dec. 81
		6. PERFORMING ORG. REPORT NUMBER
7. AUTHOR(s) W. R. Briley and H. McDonald		8. CONTRACT OR GRANT NUMBER(s) N00014-77-C-0075
9. PERFORMING ORGANIZATION NAME AND ADDRESS Scientific Research Associates, Inc. P.O. Box 498 Glastonbury, CT 06033		10. PROGRAM ELEMENT, PROJECT, TASK AREA & WORK UNIT NUMBERS
11. CONTROLLING OFFICE NAME AND ADDRESS Office of Naval Research 800 N. Quincy Street Arlington, VA 22217		12. REPORT DATE March 1982
14. MONITORING AGENCY NAME & ADDRESS (if different from Controlling Office)		13. NUMBER OF PAGES
		15. SECURITY CLASS. (of this report) Unclassified
		15a. DECLASSIFICATION DOWNGRADING SCHEDULE
16. DISTRIBUTION STATEMENT (of this Report) Approved for Public Release; Distribution Unlimited		
17. DISTRIBUTION STATEMENT (of the abstract entered in Block 20, if different from Report)		
18. SUPPLEMENTARY NOTES		
19. KEY WORDS (Continue on reverse side if necessary and identify by block number) Three-Dimensional Flow Compressible Navier-Stokes Equations Turbulent Flow Horseshoe Vortex Flow Implicit Algorithm Swept Leading Edge Nonorthogonal Coordinates		
20. ABSTRACT (Continue on reverse side if necessary and identify by block number) Three-dimensional turbulent horseshoe vortex flow past strut/endwall configurations having both unswept and 45-degree swept leading edges is studied by numerical solution of the compressible Reynolds-averaged Navier-Stokes equations. The Cartesian form of the equations is transformed to a general nonorthogonal coordinate system which is fitted to the geometry of interest and then solved using a consistently-split linearized block implicit (LBI) algorithm. The turbulence model and computational mesh provides for resolution of the viscous sublayer and employs an isotropic eddy viscosity based on solution of the turbulence kinetic		

energy equation and a specified length scale. Although no flow measurements are available for the region near the leading edge, predictions of the horseshoe vortex formation near the leading edge are in qualitative agreement with flow visualization studies of similar flows. Predictions of the relatively weak secondary flow in the corner region well downstream of the unswept leading edge do not agree with available measurements, and this is believed to be the result of numerical truncation error and/or inadequacy of the turbulence model.

ABSTRACT

Three-dimensional turbulent horseshoe vortex flow past strut/endwall configurations having both unswept and 45-degree swept leading edges is studied by numerical solution of the compressible Reynolds-averaged Navier-Stokes equations. The Cartesian form of the equations is transformed to a general nonorthogonal coordinate system which is fitted to the geometry of interest and then solved using a consistently-split linearized block implicit (LBI) algorithm. The turbulence model and computational mesh provides for resolution of the viscous sublayer and employs an isotropic eddy viscosity based on solution of the turbulence kinetic energy equation and a specified length scale. Although no flow measurements are available for the region near the leading edge, predictions of the horseshoe vortex formation near the leading edge are in qualitative agreement with flow visualization studies of similar flows. Predictions of the relatively weak secondary flow in the corner region well downstream of the unswept leading edge do not agree with available measurements, and this is believed to be the result of numerical truncation error and/or inadequacy of the turbulence model.



Accession For	
NTIS GRA&I	<input checked="" type="checkbox"/>
DTIC TAB	<input type="checkbox"/>
Unannounced	<input type="checkbox"/>
Justification	
By	
Distribution/	
Availability Codes	
Avail and/or	
Dist	Special
A	

TABLE OF CONTENTS

	Page
INTRODUCTION	1
THE PRESENT APPROACH	2
Background	3
Governing Equations	3
Coordinate System	5
Turbulence Model	5
Physical Boundary and Initial Conditions	8
SOLUTION PROCEDURE	11
Background	11
Spatial Differencing and Artificial Dissipation	12
Split LBI Algorithm	13
Linearization and Time Differencing	13
Special Treatment of Diffusive Terms	14
Consistent Splitting of the LBI Scheme	15
COMPUTED RESULTS	16
Convergence Rate	16
Results for Unswept Leading Edge	17
Results for Swept Leading Edge	19
Concluding Remarks	20
REFERENCES	21
FIGURES	23

INTRODUCTION

The flow around airfoils, struts and obstacles placed in an approaching stream with a non-uniform velocity is a fundamental three-dimensional viscous flow of considerable importance. Examples of this type of flow include the flows near an aircraft wing/fuselage junction and near a submarine hull/sail junction. Another example occurs in axial compressors and turbines, where the boundary layers which develop on the annular surfaces of the axial flow passage encounter rows of stationary and rotating blades. Other examples include the flow of a river past a bridge pier or other underwater structure and other flows past surfaces where a protuberance is of necessity present. Examples can even be found in such exotic devices as fluidic control systems.

The feature common to all such flows is that a non-uniform velocity in an approaching boundary layer meets a local region of adverse pressure gradient due to the blockage effect of the obstruction. This produces a complex flowfield consisting of boundary layer separation and the formation of one or more horseshoe vortices around the obstruction. Regions of interest include both the horseshoe vortex region at the leading edge and the corner flow region downstream of the leading edge. In the case of an airfoil or strut, this corner flow region downstream of the leading edge contains streamwise vortices which affect both the performance of the airfoil or strut themselves and also the performance of other flow devices located downstream. In flows where heat transfer is critical, the presence of the streamwise vortices causes a local thinning of boundary layers and transport of free stream fluid toward the wall in portions of the flow region. This in turn serves to increase local heat transfer rates. Order-of-magnitude increases and local heat transfer rates have been observed experimentally.

Although the horseshoe vortex flow in the region of the leading edge is of interest in its own right, it is also of considerable importance in connection with the corner flows which occur downstream. Corner flows are often viewed as an isolated problem without giving much attention to the leading edge region where the corner flows originate. In cases where leading edge effects are minimal or localized (e.g. sharp or cusped leading edges placed at zero effective incidence to the approach flow), this approach may be sufficient. It seems doubtful, however, whether corner flows in general can be divorced from the flow in the leading edge region where the corner flows are formed, if for no other reason than to determine appropriate initial conditions for a corner flow analysis.

Several experimental flow visualization studies of the horseshoe vortex flow have been performed, and these have established that the flow consists of a three-dimensional boundary layer separation in front of the obstruction followed by a vortex flow which wraps around the obstruction. Little is available in the way of detailed flow measurements (including all three velocity components) for the horseshoe vortex problem, particularly downstream of separation. The only available measurements which include the secondary velocity components appear to be the recent measurements of Mehta, Shabaka and Bradshaw [1] for an unswept leading edge at zero incidence, taken in the corner flow region well downstream of the leading edge, where the secondary flows are relatively weak. Although these measurements do not cover the leading edge region where the horseshoe vortex is formed, the measurements are nonetheless helpful in assessing computational flow predictions.

Previous analytical studies have considered the three-dimensional boundary layer flow upstream of separation (e.g., Dwyer [2]) and have used rotational inviscid flow theory to estimate secondary flows (Hawthorne [3]). The authors [4] have computed solutions of the compressible Navier-Stokes equations for laminar flow near an elliptical leading edge, including the leading edge flow separation, horseshoe vortex region, and the formation of corner flows. Solutions are given in [4] for both zero and five degree angles of incidence. In the present study, this approach is extended to encompass turbulent flow and more general geometries. Solutions are given for turbulent horseshoe vortex flow past both unswept and 45 degree swept elliptical leading edges affixed to a flat plate endwall, at zero incidence.

THE PRESENT APPROACH

Background

Because of the flow separation and horseshoe vortex flow structure, analytical approaches based on simplifications such as boundary layer theory, rotational inviscid (Euler) equations, and forward marching solution procedures do not seem adequate for this problem. Consequently, the approach being taken is the numerical solution of the compressible Reynolds-averaged Navier-Stokes equations using an efficient and non-iterative time-dependent linearized block implicit (LBI) scheme. A "zone embedding" approach is used in which the flow is computed only in a subregion of the overall flow field in the immediate vicinity of the leading edge. This approach reduces the difficulty of constructing adequate body-fitted coordinate systems and is very economical, although it can be difficult to specify boundary conditions which adequately match the embedded flow region to the surrounding flow region. A method for applying inflow/outflow boundary conditions on curved coordinate surfaces was developed in the previous study [4] of laminar horseshoe vortex flow and is also used here. These boundary conditions are derived from an assumed flow structure and physical approximations, and allow inflow of an inviscid free stream and developing boundary layer, and outflow of streamwise vorticity. The boundary conditions also transmit pressure waves through the inflow boundary during the transient process, and this avoids the instability or slow convergence often attributed to the reflection of pressure waves at an inflow boundary with fixed velocity and pressure. The equations are solved in the low Mach number regime ($M = 0.05$) for which they approximate the flow of a liquid. The methods used here have been applied in the transonic and supersonic flow regimes on other problems.

Governing Equations

The computation of flow past swept leading edge geometries requires the use of nonorthogonal coordinates. This is accomplished here by a general coordinate transformation which transforms the governing equations from a reference Cartesian coordinate system to a general nonorthogonal coordinate system which is fitted to the geometry of interest. The Cartesian velocity components u_i are retained as dependent variables in the transformed system of equations. This same technique of transforming the Cartesian system to general nonorthogonal coordinates is also used by Pulliam and Steger [6] and Shamroth, Gibelg and McDonald [7].

The transformation T from Cartesian coordinates x_i to computational coordinates y^j is given by

$$T = y^j(x_i) \quad i, j = 1, 2, 3 \quad (1)$$

Spatial derivatives are transformed according to

$$\frac{\partial}{\partial x_i} = y^j_{,i} \frac{\partial}{\partial y^j} \quad (2)$$

where unless otherwise stated the summation convention is used for repeated indices, and $y^j_{,i} \equiv \partial y^j / \partial x_i$. The coordinate system is defined by specifying the Cartesian coordinates of each computational grid point. The partial derivatives $\partial x_i / \partial y^j$ of the inverse transformation $T^{-1} = x_i(y^j)$ are then computed using three-point second-order difference formulas with uniform spacing of the computational coordinates y^j . The transformation derivatives $\partial y^j / \partial x_i$ are then computed from $\partial x_i / \partial y^j$ using standard procedures for computing derivatives of inverse functions (cf. Kaplan [5]).

Letting J denote the Jacobian determinant of the inverse transformation

$$J = \frac{\partial(x_1, x_2, x_3)}{\partial(y^1, y^2, y^3)} \quad (3)$$

and making use of the identity

$$\frac{\partial}{\partial y^j} J y^j_{,i} \equiv 0 \quad (4)$$

the governing Navier-Stokes equations are written in the following nondimensional form: The continuity equation is

$$\frac{\partial(\rho J)}{\partial t} + \frac{\partial}{\partial y^j} J y^j_{,i} \rho u_i = 0 \quad (5)$$

where ρ is density and t is time.

The k -th component of the momentum equation is given by

$$\frac{\partial(\rho u_k J)}{\partial t} + \frac{\partial}{\partial y^j} J y^j_{,i} (\rho u_i u_k + \delta_{ik} p - \tau_{ik}) = 0 \quad (6)$$

where p is pressure and the shear stress τ_{ik} is given by

$$\tau_{ik} = \frac{\mu_e}{Re} \left(y^m_{,k} \frac{\partial u_i}{\partial y^m} + y^m_{,i} \frac{\partial u_k}{\partial y^m} - \frac{2}{3} \delta_{ik} y^m_{,\ell} \frac{\partial u_\ell}{\partial y^m} \right) \quad (7)$$

Here, μ_e is a nondimensional isotropic effective viscosity coefficient which includes both laminar and turbulent contributions. Re is a reference Reynolds number, and

δ_{ik} is the Kronecker delta function.

The equation of state for a perfect gas is given by

$$p = \rho T / \gamma M^2 \quad (8)$$

where T is temperature, M is a reference Mach number, and γ is the specific heat ratio.

The total enthalpy E is defined by

$$E = T / (\gamma - 1) M^2 + q^2 / 2 \quad (9)$$

where $q^2 = \delta^{ij} u_i u_j$, and its distribution is governed by the energy equation.

Although it is not necessary, it is both convenient and computationally worthwhile for the present problem to assume that E is a constant, E_0 , and to omit solution of the energy equation. This results in negligible error for flow at low Mach number with no heat addition. Equations (8) and (9) can then be combined to produce an adiabatic equation of state

$$p = \rho (E_0 - q^2 / 2) (\gamma - 1) / \gamma \quad (10)$$

which is used to eliminate pressure as a dependent variable in Eq. (6).

Coordinate System

Perspective views of the geometry, coordinate system and computational grid for each of the two leading-edge configurations considered here are shown in Fig. 1. The coordinate system fits all solid surfaces within the computational domain but is not aligned with the direction of the free stream flow. The coordinate system is of sufficient generality to treat leading edges of arbitrary (smooth) cross-sectional shape and with a swept leading edge whose angle may vary in the spanwise direction. In each plane ($y^3 = \text{constant}$) parallel to the endwall, the coordinates consist of radial y^1 lines normal to the curve where this plane intersects the airfoil surface, and circumferential y^2 lines parallel to this curve. These coordinate planes are "sheared" by adding an arbitrary displacement $D(y^3)$ to the Cartesian x_1 coordinates for the endwall plane. Analytical coordinate transformations due to Roberts [8] were used for each coordinate direction to redistribute grid points for adequate resolution of the viscous sublayer regions on both the airfoil and endwall surfaces and of the geometric curvature near the leading edge.

Turbulence Model

The turbulence model used falls into the category of one-equation turbulence models discussed by Launder and Spalding [9], and parallels the method given by Shamroth and Gibeling [10]. This model requires solution of a single partial dif-

ferential equation governing turbulence kinetic energy k , in conjunction with a specified length scale ℓ . A turbulent viscosity μ_t is obtained from the Prandtl-Kolmogorov constitutive relationship $\mu_t \propto \ell k^{1/2}$. The turbulent viscosity μ_t is assumed to be isotropic, and the stress tensor in the ensemble-averaged equation is determined by adding the turbulent viscosity to the molecular viscosity μ to obtain the total effective viscosity $\mu_e = \mu + \mu_t$.

Specification of the length scale is the remaining task which is necessary to treat the three-dimensional horseshoe vortex flow. This flow has turbulent shear layers both on the endwall (fuselage) beginning upstream of the leading edge and also on the airfoil or strut surface (and corner region) beginning at the leading edge. Given an estimate of the mixing length at the edge of each of these shear layers and its streamwise growth rate, a distribution of mixing length within the shear layers can be obtained from semi-empirical relationships widely used in two- and three-dimensional boundary layer calculations. To estimate the growth rate of the two shear layers, a boundary layer momentum integral procedure is used for each type of shear layer. Wind tunnel blockage effects are included in the endwall shear layer calculation, and turbulent transition is presumed to occur at the leading edge in the airfoil shear layer calculation. The final turbulence model provides for resolution of the viscous sublayer region near walls, and permits calculation of the separated horseshoe vortex regions near the leading edge and in the corner.

The equation governing turbulence kinetic energy is given by Launder and Spalding [11] for Cartesian coordinates. Applying the general coordinate transformation (1), this equation can be written as

$$\frac{\partial(\rho k J)}{\partial t} + \frac{\partial}{\partial y^j} J y^j_{,i} \left[\rho u_i k - \frac{1}{\text{Re}} \left(\mu + \frac{\mu_t}{\sigma_k} \right) y^m_{,i} \frac{\partial k}{\partial y^m} \right] = \quad (11)$$

$$J \frac{\mu_t}{\text{Re}} \left[2 D_{ij} D_{ij} - \frac{2}{3} \left(y^j_{,i} \frac{\partial u_i}{\partial y^j} \right)^2 \right] - \frac{1}{\text{Re}} J \epsilon$$

where

$$D_{ij} = y^m_{,i} \frac{\partial u_i}{\partial y^m} + y^m_{,i} \frac{\partial u_j}{\partial y^m} \quad (12)$$

Here, ϵ is the turbulence dissipation rate and σ_k is the turbulent Prandtl number (taken here as 1.0).

The turbulent viscosity is obtained from the Prandtl-Kolmogorov relation

$$\mu_t = c_\mu \rho k^2 / \epsilon = c_\mu^{1/4} \rho k^{1/2} \epsilon^{1/4} \quad (13)$$

where the dissipation rate is given by

$$\epsilon = c_\mu^{3/4} k^{3/2} / \lambda \quad (14)$$

For high Reynolds number flow, c_μ is approximately 0.09. For low Reynolds number and in the viscous sublayer, c_μ is given a prescribed dependence on turbulence Reynolds number R_t in the manner suggested by McDonald and Fish [12] for transitional boundary layer flows. In [12], the turbulence Reynolds number R_t was appropriately defined as an integral average across the boundary layer. Here and following [10], it is convenient to define R_t as the local ratio of turbulent to laminar viscosity $R_t = \mu_t / \mu$. The structural coefficient c_μ is given in [12] as $c_\mu = 4(a_1)^2$, where

$$a_1 = a_0 f(R_t) / [1 + 6.66 a_0 (f(R_t) - 1)] \quad (15)$$

where $a_0 = 0.0115$ and

$$f(R_t) = \begin{cases} R_t^{0.22} & R_t \leq 1 \\ 6.81 R_t + 6.143 & R_t \geq 40 \end{cases} \quad (16)$$

with a cubic polynomial curve fit for values of R_t between 1 and 40.

It remains to specify a length scale distribution appropriate for the problem under consideration. The horseshoe-vortex/corner flow of interest here has moderately thin shear layers on the endwall and strut surface, and the length scale distribution is thus adapted from previous turbulence models for turbulent boundary layers and taken to be the conventionally defined mixing length of Prandtl. The distribution of mixing length given by McDonald and Fish [12] has proven effective for a wide range of two-dimensional turbulent boundary layers and is easily adapted for present use. This distribution is given by

$$\ell = \mathcal{D} \ell_\infty \tanh(\kappa d / \ell_\infty) \quad (17)$$

where ℓ is mixing length, ℓ_∞ is an outer-region value of mixing length, d is distance from the wall, κ is the von Karman constant (taken here as 0.41), and \mathcal{D} is a sublayer damping function given by

$$\mathcal{D} = P^{1/2} [(d^+ - 23)/8] \quad (18)$$

Here, P is the normal probability function and d^+ is defined by $d^+ = d(\tau/\nu)^{1/2}/\nu$, where τ is shear stress and ν is kinematic viscosity. For equilibrium boundary layers,

ℓ_∞ is observed to have a constant value of about 0.09δ , where δ is the local boundary layer thickness.

The length scale distribution of Eq. (17) is adapted for present use by taking d as distance to the nearest wall and by assigning ℓ_∞ a distribution based on two-dimensional momentum integral estimates of the boundary layer growth rates on the endwall and on the strut. The computed estimates of boundary layer growth were obtained from a simple integral prediction scheme rather than an attempt to scan the intermediate transient solutions of the Navier-Stokes equations to determine some ill-defined boundary layer thickness. Assuming a $1/7$ power law velocity profile and a skin friction law $c_f/2 = 0.0225 (\nu/u_e \delta)^{1/4}$, the momentum integral equation can be written as

$$h_1 \frac{d\delta}{dx} + h_2 \frac{\delta}{u_e} \frac{du_e}{dx} = c_f/2 \quad (19)$$

where for the $1/7$ power profile: $h_1 = 7/72$ and $h_2 = 23/72$. The momentum integral equation is applied to both strut and endwall boundary layers. The free stream velocity u_e is imposed from a potential flow. The flow cases computed here are enclosed in a wind tunnel, and since the endwall boundary layer causes blockage effects in this instance, the free stream velocity is adjusted for this effect. If distances are normalized by the tunnel half-height, then the free stream velocity adjusted for blockage is given by $u_e = 1/(1-\delta^*)$, where for the $1/7$ power velocity profile, the displacement thickness δ^* is related to δ by $\delta = 8 \delta^*$. This relationship for u_e is inserted into Eq. (19) prior to solution. Eq. (19) is solved using a second-order linearized finite difference scheme described in [13].

Two boundary layer thickness distributions, $\delta_1(x_1)$ for the endwall boundary layer and $\delta_2(y^2)$ for the strut surface, are obtained by solution of Eq. (19). An outer or maximum mixing length scale associated with each boundary layer is determined from the formula $\ell_\infty = 0.09 \delta$. In the core region outside the boundary layer, the length scale is exponentially damped to a negligible value over a distance of about two boundary layer thicknesses. In the overlap corner region, the outer or maximum length scale ℓ_∞ is taken as the greater of the two values associated with the strut and endwall boundary layers.

Physical Boundary and Initial Conditions

Since the computational domain is chosen to be a region in the immediate vicinity of the leading-edge/corner flow geometry (cf. Fig. 1) embedded within a larger overall flow system, inflow and outflow boundary conditions which adequately model the interface between the computed flow and the remainder of the flow system are required.

The inflow/outflow conditions used are derived from an assumed flow structure and are chosen to provide inflow with prescribed stagnation pressure (and stagnation enthalpy) in an inviscid core region and with a given axial velocity profile shape in the endwall boundary layer, and to provide outflow with a prescribed distribution of static pressure in the cross section. These boundary conditions are compatible both with an inviscid characteristics analysis and with the physical process by which most flows are established. These boundary conditions allow both velocity and static pressure to vary with time at the inflow boundary, and consequently, pressure waves are transmitted upstream through the inflow boundary during the transient flow process and are not reflected back into the computational domain. The reflection of pressure waves at an inflow boundary where velocity and pressure are fixed in time has often been cited as a cause of either instability or slow convergence in other investigations. These boundary conditions are discussed in more detail in [14].

The initial and boundary conditions are devised from a rough approximation of the two-dimensional potential flow velocity \bar{U}_I for the strut cross section, and from the momentum-integral estimates for blockage $B(x_1)$ and for the boundary layer thickness distributions $\delta_1(x_1)$ and $\delta_2(y^2)$ on the endwall flat plate and strut surfaces, respectively. Finally, boundary layer velocity profile shapes $f_1(\bar{y}/\delta_1)$ and $f_2(\bar{y}/\delta_2)$, $0 \leq f_1$, $f_2 \leq 1$ are defined, where \bar{y} is a parameter indicative of distance from a wall. These velocity profile shapes were taken from the analytical fit of Musker [15] to the Coles-type of profile which matches δ^* and c_f from the momentum-integral calculations. The initial conditions at time $t = 0$ are defined by

$$\bar{U} = \bar{U}_I B(x_1) f_1(\bar{y}/\delta_1) f_2(\bar{y}/\delta_2) \quad (20)$$

$$c_p = 1 - B^2 \bar{U}_I \cdot \bar{U}_I \quad (21)$$

where \bar{U} is the velocity vector and c_p is the pressure coefficient referred to the reference conditions. The details of this procedure are not critical and are omitted, since except for the shape and thickness of the inlet boundary layer profile, these results serve only as a convenient method for selecting initial conditions. A reasonably accurate estimate for the pressure drop which will produce the desired flow rate must be made using any convenient source. For the present problem, the approximate potential flow corrected for blockage as in Eq. (21) is adequate. It is noted that although these initial conditions do take into account several relevant features of the flow, the important effects of flow separation, and horseshoe/corner vortex formation are completely neglected. The initial flow field is thus a simple but relatively crude approximation to the final flow field.

At the inflow boundary $y^1 = y^1_{\max}$, a "two-layer" boundary condition is employed as in [4], such that stagnation pressure p_0 is fixed at the free stream reference value in the core flow region ($y^3 > \delta_1$) and the axial velocity profile shape $u_1/u_e = f_1(\bar{y}/\delta_1)$ is fixed within the boundary layer region ($y^3 \leq \delta_1$). Here, u_e is the local edge velocity which varies with time and is adjusted after each time step to the value consistent with p_0 and the local edge static pressure, which is determined as part of the solution. The remaining inflow conditions are $u_2 = \partial^2 u_3 / \partial n^2 = \partial^2 c_p / \partial n^2 = 0$, where n denotes the normal computational coordinate, y^1 . For outflow conditions, the static pressure is imposed, and second derivatives of each velocity component are set to zero.

At no-slip surfaces, each velocity component u_i is set to zero, and the remaining condition applied at these surfaces is that the derivative of pressure in the direction normal to the surface is zero. This condition approximates the normal momentum equation to order Re^{-1} for viscous flow at a no-slip surface. For the swept leading edge configuration, the surface normal does not always lie on a coordinate line, and the normal derivative boundary condition must be derived from the coordinate transformation data. Letting $\bar{e}_j = \partial \bar{r} / \partial y^j$ denote the basis vectors for y^j , where \bar{r} is the position vector, then the unit vector \bar{n} normal to the $y^1 - y^2$ coordinate surface is given by $\bar{n} = \bar{e}_1 \times \bar{e}_2 / |\bar{e}_1 \times \bar{e}_2|$. If n^i are the Cartesian components of \bar{n} , then the normal derivative of ϕ is given by

$$\bar{n} \cdot \nabla \phi = n^i y^j_{,i} \frac{\partial \phi}{\partial y^j} \quad (22)$$

The final boundary to be considered is the plane parallel to the endwall and in the free stream. This boundary is assumed to be a plane of symmetry, so that the flow represented is that past the strut mounted between parallel flat plates with spacing $2H$. This assumption is both convenient and corresponds to the conditions in the wind tunnel experiment for the unswept leading edge flow, for which experimental measurements are available.

SOLUTION PROCEDURE

Background

The solution procedure employs a consistently-split linearized block implicit (LBI) algorithm which has been discussed in detail by the authors in [13, 16]. There are two important elements of this method:

- (1) the use of a noniterative formal time linearization to produce a fully-coupled linear multidimensional scheme which is written in "block implicit" form; and
- (2) solution of this linearized coupled scheme using a consistent "splitting" (ADI scheme) patterned after the Douglas-Gunn [17] (1964) treatment of scalar ADI schemes.

The method is thus referred to as a split linearized block implicit (LBI) scheme.

The method has several attributes:

- (1) the noniterative linearization is efficient;
- (2) the fully-coupled linearized algorithm eliminates instabilities and/or extremely slow convergence rates often attributed to methods which employ ad hoc decoupling and linearization assumptions to identify nonlinear coefficients which are then treated by lag and update techniques;
- (3) the splitting or ADI technique produces an efficient algorithm which is stable for large time steps and also provides a means for convergence acceleration for further efficiency in computing steady solutions;
- (4) intermediate steps of the splitting are consistent with the governing equations, and this means that the "physical" boundary conditions can be used for the intermediate solutions. Other splittings which are inconsistent can have severe difficulties in satisfying physical boundary conditions [13].
- (5) the convergence rate and overall efficiency of the algorithm are much less sensitive to mesh refinement and redistribution than algorithms based on explicit schemes or which employ ad hoc decoupling and linearization assumptions. This is important for accuracy and for computing turbulent flows with viscous sublayer resolution; and

- (6) the method is general and is specifically designed for the complex systems of equations which govern viscous flow in complicated geometries.

This same algorithm was later considered by Beam and Warming [18], but the ADI splitting was derived by approximate factorization instead of the Douglas-Gunn procedure. They refer to the algorithm as a "delta form" approximate factorization scheme. This scheme replaced an earlier non-delta form scheme [19], which has inconsistent intermediate steps.

Spatial Differencing and Artificial Dissipation

The spatial differencing procedures used are a straightforward adaptation of those used in [16] and elsewhere. Three-point central difference formulas are used for spatial derivatives, including the first-derivative convection and pressure gradient terms. This has an advantage over one-sided formulas in flow calculations subject to "two-point" boundary conditions (virtually all viscous or subsonic flows), in that all boundary conditions enter the algorithm implicitly. In practical flow calculations, artificial dissipation is usually needed and is added to control high-frequency numerical oscillations which otherwise occur with the central-difference formula.

In the present investigation, artificial (anisotropic) dissipation terms of the form

$$\sum_{i,j} d_j \nabla_j (y_{,i}^j)^2 \frac{\partial^2 u_k}{\partial y^j \partial y^j} \quad (23)$$

are added to the right-hand side of each (k-th) component of the momentum equation (6), where for each coordinate direction y^j , the artificial diffusivity d_j is positive and is chosen as the larger of zero and the local quantity $\mu_e (\sigma \text{Re}_{\Delta y^j} - 1)/\text{Re}$. Here, the local cell Reynolds number $\text{Re}_{\Delta y^j}$ for the j-th direction is defined by

$$\text{Re}_{\Delta y^j} = \text{Re} \left| \sum_i y_{,i}^j \rho u_i \right| \Delta y^j / \mu_e \sum_i (y_{,i}^j)^2 \quad (24)$$

with no summation on j. This treatment lowers the formal accuracy to $O(\Delta x)$, but the functional form is such that accuracy in representing physical shear stresses in thin shear layers with small normal velocity is not seriously degraded. This latter property follows from the anisotropic form of the dissipation and the combination of both small normal velocity and small grid spacing in thin shear layers. A value of 0.5 was used for σ in the present calculations. Values lower than 0.5 have been used to good effect in two space dimensions [20, 21], but it has not yet been possible to investigate the role of smaller σ values in three space dimensions.

Split LBI Algorithm

Linearization and Time Differencing

The system of governing equations to be solved consists of continuity (5), three components of momentum (6) and the turbulence kinetic energy equation (11). Ancillary relations (10) and (14) are substituted in these equations to eliminate p and ϵ as dependent variables. This produces a system of five equations in five dependent variables: ρ , u_1 , u_2 , u_3 , and k . Using notation similar to that in [16], at a single grid point this system of equations can be written in the following form:

$$\partial H(\phi)/\partial t = D(\phi) + S(\phi) \quad (25)$$

where ϕ is the column-vector of dependent variables, H and S are column-vector algebraic functions of ϕ , and D is a column vector whose elements are the spatial differential operators which generate all spatial derivatives appearing in the governing equation associated with that element. In the present case, the only non-zero element in S is generated by the last term in the turbulence kinetic energy equation (11).

The solution procedure is based on the following two-level implicit time-difference approximations of (25):

$$(H^{n+1} - H^n)/\Delta t = \beta(D^{n+1} + S^{n+1}) + (1-\beta)(D^n + S^n) \quad (26)$$

where, for example, H^{n+1} denotes $H(\phi^{n+1})$ and $\Delta t = t^{n+1} - t^n$. The parameter β ($0.5 \leq \beta \leq 1$) permits a variable time-centering of the scheme, with a truncation error of order $[\Delta t^2, (\beta - 1/2) \Delta t]$.

A local time linearization (Taylor expansion about ϕ^n) of requisite formal accuracy is introduced, and this serves to define a linear differential operator L (cf. [16]) such that

$$D^{n+1} = D^n + L^n (\phi^{n+1} - \phi^n) + O(\Delta t^2) \quad (27)$$

Similarly,

$$H^{n+1} = H^n + (\partial H/\partial \phi)^n (\phi^{n+1} - \phi^n) + O(\Delta t^2) \quad (28)$$

$$S^{n+1} = S^n + (\partial S/\partial \phi)^n (\phi^{n+1} - \phi^n) + O(\Delta t^2) \quad (29)$$

Eqs. (27-29) are inserted into Eq. (26) to obtain the following system which is linear in ϕ^{n+1} :

$$(A - \beta \Delta t L^n) (\phi^{n+1} - \phi^n) = \Delta t (D^n + S^n) \quad (30)$$

and which is termed a linearized block implicit (LBI) scheme.

Here, A denotes a square matrix defined by

$$A \equiv (\partial H / \partial \phi)^n - \beta \Delta t (\partial S / \partial \phi)^n \quad (31)$$

Eq. (30) has $O(\Delta t)$ accuracy unless $H \equiv \phi$, in which case the accuracy is the same as Eq. (26).

Special Treatment of Diffusive Terms

The time differencing of diffusive terms is modified to accomodate cross-derivative terms and also turbulent viscosity and artificial dissipation coefficients which depend on the solution variables. Although formal linearization of the convection and pressure gradient terms and the resulting implicit coupling of variables is critical to the stability and rapid convergence of the algorithm, this does not appear to be important for the turbulent viscosity and artificial dissipation coefficients. Since the relationship between μ_e and d_j and the mean flow variables is not conveniently linearized, these diffusive coefficients are evaluated explicitly at t^n during each time step. Notationally, this is equivalent to neglecting terms proportional to $\partial \mu_e / \partial \phi$ or $\partial d_j / \partial \phi$ in L^n , which are formally present in the Taylor expansion (27), but retaining all terms proportional to μ_e or d_j in both L^n and D^n .

It has been found through extensive experience that this has little if any effect on the performance of the algorithm. This treatment also has the added benefit that the turbulence model equations (in this instance the turbulence kinetic energy equation) can be decoupled from the system of mean flow equations by an appropriate matrix partitioning (cf. [13]) and solved separately in each step of the ADI solution procedure. This reduces the block size of the block tridiagonal systems which must be solved in each step and thus reduces the computational labor.

In addition, the viscous terms in the present formulation include a number of spatial cross-derivative terms. Although it is possible to treat cross-derivative terms implicitly within the ADI treatment which follows, it is not at all convenient to do so, and consequently, all cross-derivative terms are evaluated explicitly at t^n . For a scalar model equation representing combined convection and diffusion, it has been shown by Beam and Warming [22] that the explicit treatment of cross-derivative terms does not degrade the unconditional stability of the present algorithm. To preserve notational simplicity, it is understood that all cross-derivative terms appearing in L^n are neglected but are retained in D^n . It is important to note that neglecting terms in L^n has no effect on steady solutions of Eq. (30), since $\phi^{n+1} - \phi^n \equiv 0$ and thus Eq. (30) reduces to the steady form of the equations: $D^n + S^n = 0$. Aside from stability considerations, the only effect of neglecting terms in L^n is to introduce an $O(\Delta t)$ truncation error.

Consistent Splitting of the LBI Scheme

To obtain an efficient algorithm, the linearized system (30) is split using ADI techniques. To obtain the split scheme, the multidimensional operator L is rewritten as the sum of three "one-dimensional" sub-operators L_i ($i = 1, 2, 3$) each of which contains all terms having derivatives with respect to the i -th spatial coordinate. The split form of Eq. (30) can be derived either as in [13, 16] by following the procedure described by Douglas and Gunn [17] in their generalization and unification of scalar ADI schemes, or using approximate factorization as in [18]. For the present system of equations, the split algorithm is given by

$$(A - \beta \Delta t L_1^n) (\phi^* - \phi^n) = \Delta t (D^n + S^n) \quad (32a)$$

$$(A - \beta \Delta t L_2^n) (\phi^{**} - \phi^n) = A (\phi^* - \phi^n) \quad (32b)$$

$$(A - \beta \Delta t L_3^n) (\phi^{n+1} - \phi^n) = A (\phi^{**} - \phi^n) \quad (32c)$$

where ϕ^* and ϕ^{**} are consistent intermediate solutions [13, 16]. If spatial derivatives appearing in L_i and D are replaced by three-point difference formulas, as indicated previously, then each step in Eqs. (32a-c) can be solved by a block-tridiagonal elimination.

Combining Eqs. (32a-c) gives

$$\begin{aligned} & (A - \beta \Delta t L_1^n) A^{-1} (A - \beta \Delta t L_2^n) A^{-1} (A - \beta \Delta t L_3^n) (\phi^{n+1} - \phi^n) \\ & = \Delta t (D^n + S^n) \end{aligned} \quad (33)$$

which approximates the unsplit scheme (30) to $O(\Delta t^2)$. Since the intermediate steps are also consistent approximations for Eq. (30), physical boundary conditions can be used for ϕ^* and ϕ^{**} [13, 16]. Finally, since the L_i are homogeneous operators, it follows from Eqs. (32a-c) that steady solutions have the property that $\phi^{n+1} = \phi^* = \phi^{**} = \phi^n$ and satisfy

$$D^n + S^n = 0 \quad (34)$$

The steady solution thus depends only on the spatial difference approximation used for (34) and does not depend on the solution algorithm itself.

COMPUTED RESULTS

Solutions for three-dimensional turbulent flow past both unswept and 45-degree swept elliptical leading edges affixed to a flat plate endwall are presented here. To assess the degree of accuracy obtainable in three-dimensional flow calculations, it is obviously valuable to have experimental measurements for comparison. The recent measurements by Mehta, Shabaka and Bradshaw [1] for turbulent corner flow downstream of an unswept elliptical leading edge at zero incidence appear to be the only measurements available which include secondary velocity components, and this flow was selected for computation.

Solutions were computed for turbulent horseshoe vortex flow past both unswept and 45-degree swept leading edges having the configurations shown in Fig. 1, each having a Reynolds number $Re = 130,000$ and Mach number $M = 0.05$. The grids used were $18 \times 28 \times 18$ and $18 \times 24 \times 21$ (y^1, y^2, y^3) for the unswept and swept cases, respectively. The Reynolds number is based on the tunnel half-height of 2.5 inches. The geometry consists of an elliptical leading edge with a half-chord of 6 inches, followed by a slab with constant thickness of 2 inches. In the configuration with swept leading edge, this cross section is "sheared" as shown in Fig. 1b to form a sweep angle of 45 degrees at the endwall. The angle of sweep varies smoothly between 45 degrees at the endwall and zero degrees at the symmetry plane midway between the wind tunnel walls. This particular swept configuration was selected to produce a flow which is symmetric about this midplane, for ease in imposing boundary conditions. Mehta, Shabaka and Bradshaw indicate that the boundary layer on the endwall has a thickness of approximately 1.0 inches at the leading edge; momentum integral calculations were used to estimate an inflow boundary layer thickness which would match this condition.

Convergence Rate

Turbulent flows, particularly in three dimensions, are especially difficult to compute because of the very high degree of mesh redistribution required to resolve viscous sublayer regions. Resolution of the viscous sublayer is believed necessary to obtain an adequate representation of the turbulent shear layer behavior. In addition, because of the leading-edge geometry and the high strut length-to-thickness aspect ratio, this mesh redistribution is required for all three coordinate directions. This contrasts, for example, with three-dimensional flow in a curved pipe or duct, where only one or two (respectively) coordinate directions require substantial mesh redistribution. As a consequence, the ratio of largest to smallest elemental

control volume for the present calculation is approximately 3×10^9 . The corresponding matrix of difference approximations has an extremely wide range of eigenvalues, and thus poses a computational problem for which rapid convergence is difficult to achieve.

The present computational method employs variable time steps to accelerate convergence, as discussed in [23]. Several procedures for time step selection are presently under evaluation, but typically small time steps are used initially during the elimination of impulsive transients, followed by larger time steps and the cyclic use of a sequence of time steps. In addition, a smaller time step was used near the leading edge than elsewhere in the flow field. Small time steps are effective in reducing high (spatial) frequency error components, while large time steps are effective in reducing low frequency errors.

An indication of both the degree and rate of convergence obtained for the present calculations is shown in Fig. 2. For comparison, a curve representative of the convergence behavior typically obtained for two-dimensional turbulent flow cases is also shown. Although the present convergence rate is noticeably slower than that observed using this same algorithm in other calculations, it is adequate for present purposes. The present calculations were terminated after approximately 100 iterations for reasons of economy, since it appeared that changes in the solution at this point were of minor significance and would not alter any of the conclusions drawn from these results.

Results for Unswept Leading Edge

Computed results for the unswept leading-edge case are given in a series of plots in Figs. 3 - 10. It is difficult to display graphically the results of three-dimensional flow calculations, and the present approach is to consider contour and velocity vector plots for selected two-dimensional planes and projected surfaces, which are representative of the computed flow structure. Because of the multiple length scales in these results, the solutions are plotted in some instances for the entire computational region and grid, and in other instances only a portion of the computed solution is shown. Grid point indices are used in these plots as a means of identifying the extent of the region shown. The notation x, y, z is used to denote the respective computational coordinates y^i shown in Fig. 1.

In Fig. 3, the coordinates and computational grid are shown for planes which are parallel to the endwall. In Figs. 4 and 5, velocity vector plots from the nominally two-dimensional flow region at the free stream symmetry plane midway between the tunnel walls are contrasted with the corresponding results at the plane of grid points adjacent to the endwall and very near the endwall surface. The vector

magnitudes are renormalized for each plot and thus indicate only flow direction and relative magnitude within the plot. In this region near the leading edge, the computed flow structure has all of the characteristics observed in numerous flow visualization experiments and in the authors' previous laminar calculations [4]. The flow near the endwall separates and forms a horseshoe vortex upstream of the leading edge with peak reverse flow velocity in this instance about 20 per cent of the free stream velocity. The reversed flow within the horseshoe vortex is clearly evident in Fig. 5. A secondary vortex can also be seen at the leading edge, but this is only marginally resolved.

In Fig. 6, the static pressure and velocity are shown for the (vertical) stagnation flow plane containing the leading edge and extending upstream parallel to the freestream flow. The horseshoe vortex is too small and too close to the leading edge to be visible on the scale of Fig. 6, but is shown in Fig. 7 in a detail of the region near the intersection of the leading edge and endwall. The peak velocity is directed toward the endwall and parallel to the leading edge, and is about 35 per cent of the freestream velocity.

A full scale view of the axial velocity and secondary or crossflow velocity is shown in Fig. 8 for the plane perpendicular to the corner intersection and located at the end of the elliptical leading edge region (the $y = 20$ plane, cf. Fig. 3). Details of the corner flow downstream of the leading edge are shown in Figs. 9 and 10 at each of three axial locations (see Fig. 3 for locations). The growth of the corner shear layer and a rapid decay of the secondary flow strength can be seen in Figs. 9 and 10. The last axial location shown ($y = 26$) corresponds approximately to axial station 2 (Fig. 1a) for which measurements of both axial and transverse velocities were taken by Mehta, Shabaka and Bradshaw [1]. Their measurements are shown in Fig. 11, and in this region (about 25 inches downstream of the leading edge) the measurements show a single corner vortex having the same sense as that computed near the leading edge but with a peak cross flow velocity of about 5 per cent of the free stream velocity. The computed cross flow does not agree well with measurements in this region, however, and indicates that the corner vortex flow has very small cross flow velocities (less than 0.5 per cent of free stream velocity), and of opposite sense. This poor agreement is presumably the result of numerical truncation error and/or inadequacy of the turbulence model. It is not possible to make any further quantitative assessment on the basis of the available measurements alone. It is unfortunate that experimental measurements were not taken near the leading edge, and thus comparisons cannot be made in this critical region where the vortex is formed.

Related difficulties have been encountered in obtaining accurate three-dimensional flow predictions for flow in curved ducts [24], and in that study, the turbulence model does not appear to be responsible. It is believed that the present disagreement with experiment is most likely the result of numerical error including the added artificial dissipation. In a recent investigation of two-dimensional viscous transonic flow past airfoils [20], it was found that significant reductions in the magnitude (factors of 10 to 20) of the artificial dissipation are possible without destabilizing the calculation and with a corresponding increase in accuracy. The present calculation was repeated with a tenfold reduction in dissipation parameter but was found to be unstable. Further work is needed to resolve the present discrepancy between prediction and experiment.

Results for Swept Leading Edge

Computed results for the 45-degree swept leading edge configuration in Fig. 1b are given in Figs. 12 - 21. This flow also separates and forms a horseshoe vortex upstream of the leading edge. The computed flow structure for the swept geometry differs from that for the unswept geometry in two important respects. First, the strength of the horseshoe vortex at the leading edge is significantly reduced by the swept leading edge, as evidenced by a peak reverse flow velocity of approximately 10 per cent of the free stream velocity (compared with 20 per cent for the unswept geometry). Secondly, outside the horseshoe vortex region, a cross flow parallel to the swept leading edge and directed outward away from the endwall occurs due to the swept geometry. The peak velocity parallel to the swept leading edge is predicted to be approximately 40 per cent of the free stream velocity. This cross flow disappears downstream of the swept leading edge and is completely absent in the unswept geometry.

The grid distribution used for this case is shown in Fig. 12. Side-view projections of the flow near the surface of the strut are shown in Fig. 13 (entire grid) and in Fig. 14 (detail near leading edge). The large cross flow parallel to the swept leading edge is evident in each of these figures. Computed results for the stagnation plane upstream of the leading edge are shown in Fig. 15 (entire grid) and Fig. 16 (detail near intersection of leading edge and endwall). Computed distributions of velocity and pressure are given in Fig. 16 for a plane parallel to the flat plate and located near the edge of the flat plate boundary layer. Details of the flow near the leading edge are shown in Figs. 18 and 19 for the free stream symmetry plane and for the plane of grid points adjacent to the endwall surface. The reversed flow region inside the horseshoe vortex is clearly visible in Fig. 19.

Finally, projections of the corner flow downstream of the leading edge are shown in Figs. 20 and 21 at each of three axial locations (see Fig. 12 for location).

To summarize these results, the computed flow field near the swept leading edge displays a reduced vortex strength, strong cross flow along the swept leading edge, and a modified pressure distribution near the strut-endwall intersection. Although these flow characteristics are qualitatively what one expects for this flow, no other analytical or experimental results are available for quantitative evaluation, and at this point the results serve mainly as a demonstration of capability for computing this complex and difficult three-dimensional turbulent horseshoe vortex flow.

Concluding Remarks

Three-dimensional turbulent horseshoe vortex flow past both swept and unswept leading-edge/endwall configurations has been studied by numerical solution of the Reynolds-averaged Navier-Stokes equations. It is believed that the physical processes involved require the viscous sublayer to be resolved, and the computational approach provides for this resolution and has been used with general nonorthogonal coordinates.

Predictions of the horseshoe vortex formation near the leading edge are in qualitative agreement with flow visualization studies of similar flows. No flow measurements are available for the region near the leading edge. Predictions of the relatively weak secondary flows in the corner downstream of the unswept leading edge do not agree with available measurements well downstream of the leading edge. This disagreement is believed to be mainly the result of numerical error including that due to artificial dissipation which is used to stabilize the solution procedure. Although there is undoubtedly room for further evaluation and development of the turbulence model being used, improvement in the numerical accuracy with which these flows can be computed is needed before this can be undertaken.

REFERENCES

1. Mehta, R.D., Shabaka, I.M.M.A. and Bradshaw, P.: Embedded Longitudinal Vortices in Turbulent Boundary Layers. Symposium on Numerical and Physical Aspects of Aerodynamic Flows, Cal. State Univ., 1981.
2. Dwyer, H.A.: Calculation of Three Dimensional and Time Dependent Boundary Layer Flows. AIAA Paper No. 68-740, 1968.
3. Hawthorne, W.R.: The Secondary Flow About Struts and Airfoils. J. Aero. Sci., Vol. 21, 1954, p. 588.
4. Briley, W.R. and McDonald, H.: Computation of Three Dimensional Horseshoe Vortex Flow Using the Navier-Stokes Equations. Proc. Seventh Int. Conf. on Num. Methods in Fluid Dyn., Stanford 1980.
5. Kaplan, W.: Advanced Calculus. Addison-Wesley Publishing Company, Inc., 1952.
6. Pulliam, T.H. and Steger, J.L.: On Implicit Simulations of Three-Dimensional Flow. AIAA Paper No. 78-10, 1978.
7. Shamroth, S.J., Gibeling, H.J. and McDonald, H.: A Navier-Stokes Solution for Laminar and Turbulent Flow Through a Cascade of Airfoils. AIAA Paper No. 80-1426, 1980.
8. Roberts, G.O.: Computational Meshes for Boundary Layer Problems. Proc. 2nd Int. Conf. Num. Meth. Fluid Dynamics, (Springer-Verlag), 1971, p. 171.
9. Launder, B.E. and Spalding, D.B.: Mathematical Models of Turbulence. Academic Press, 1972.
10. Shamroth, S.J. and Gibeling, H.J.: The Prediction of the Turbulent Flow Field About an Isolated Airfoil, AIAA Paper 79-1543, 1979. Also, NASA CR 3183, 1979.
11. Launder, B.E. and Spalding, D.B.: The Numerical Computation of Turbulent Flows. Computer Methods in Applied Mechanics and Engineering, Vol. 3, 1974, p. 269.
12. McDonald, H. and Fish, R.W.: Practical Calculations of Transitional Boundary Layers. International Journal of Heat and Mass Transfer, Vol. 16, No. 9, 1973, pp. 1729-1744.
13. Briley, W.R. and McDonald, H.: On the Structure and Use of Linearized Block ADI and Related Schemes. J. Comp. Physics, Vol. 34, 1980, p. 54.
14. McDonald, H. and Briley, W.R.: Some Observations on Numerical Solutions of the Three-Dimensional Navier-Stokes Equations. Symposium on Numerical and Physical Aspects of Aerodynamic Flows. Cal. State Univ. (Long Beach), 1981.
15. Musker, A.J.: Explicit Expression for the Smooth Wall Velocity Distribution in a Turbulent Boundary Layer. AIAA Journal, Vol. 17, 1979, p. 655.
16. Briley, W.R. and McDonald, H.: Solution of the Multidimensional Compressible Navier-Stokes Equations by a Generalized Implicit Method. J. of Comp. Physics, Vol. 24, Aug. 1977, p. 372.

17. Douglas, J. and Gunn, J.E.: A General Formulation of Alternating Direction Methods. *Numerische Math.*, Vol. 6, 1964, p. 428.
18. Beam, R.M. and Warming, R.F.: An Implicit Factored Scheme for the Compressible Navier-Stokes Equations. *AIAA Journal*, Vol. 16, April 1978, p. 393.
19. Beam, R.M. and Warming, R.F.: An Implicit Finite-Difference Algorithm for Hyperbolic Systems in Conservation Law Form. *Journal of Computational Physics*, Vol. 22, Sept. 1976, p. 87.
20. Shamroth, S.J., McDonald, H. and Briley, W.R.: A Navier-Stokes Solution for Transonic Flow Through a Cascade. SRA Report R79-920007-F, 1979.
21. McDonald, H., Shamroth, S.J. and Briley, W.R.: Transonic Flows with Viscous Effects. *Transonic Shock and Multidimensional Flows: Advances in Scientific Computing*. R. E. Meyer, Ed., Academic Press, New York, 1982.
22. Beam, R.M. and Warming, R.F.: Alternating Direction Implicit Methods for Parabolic Equations with a Mixed Derivative. *SIAM J. Sci. Stat. Comp.*, Vol. 1, 1980, p. 131.
23. McDonald, H. and Briley, W.R.: Computational Fluid Dynamic Aspects of Internal Flows. AIAA Paper No. 79-1445, 1979.
24. Buggeln, R.C., Briley, W.R. and McDonald, H.: Solution of the Navier-Stokes Equations for Three-Dimensional Turbulent Flow with Viscous Sublayer Resolution. AIAA Paper No. 81-1023, 1981.

FIG. 1

GEOMETRY AND COORDINATE SYSTEM
(ELLIPTICAL LEADING EDGE WITH
RECTANGULAR AFTERBODY, ATTACHED TO FLAT PLATE)

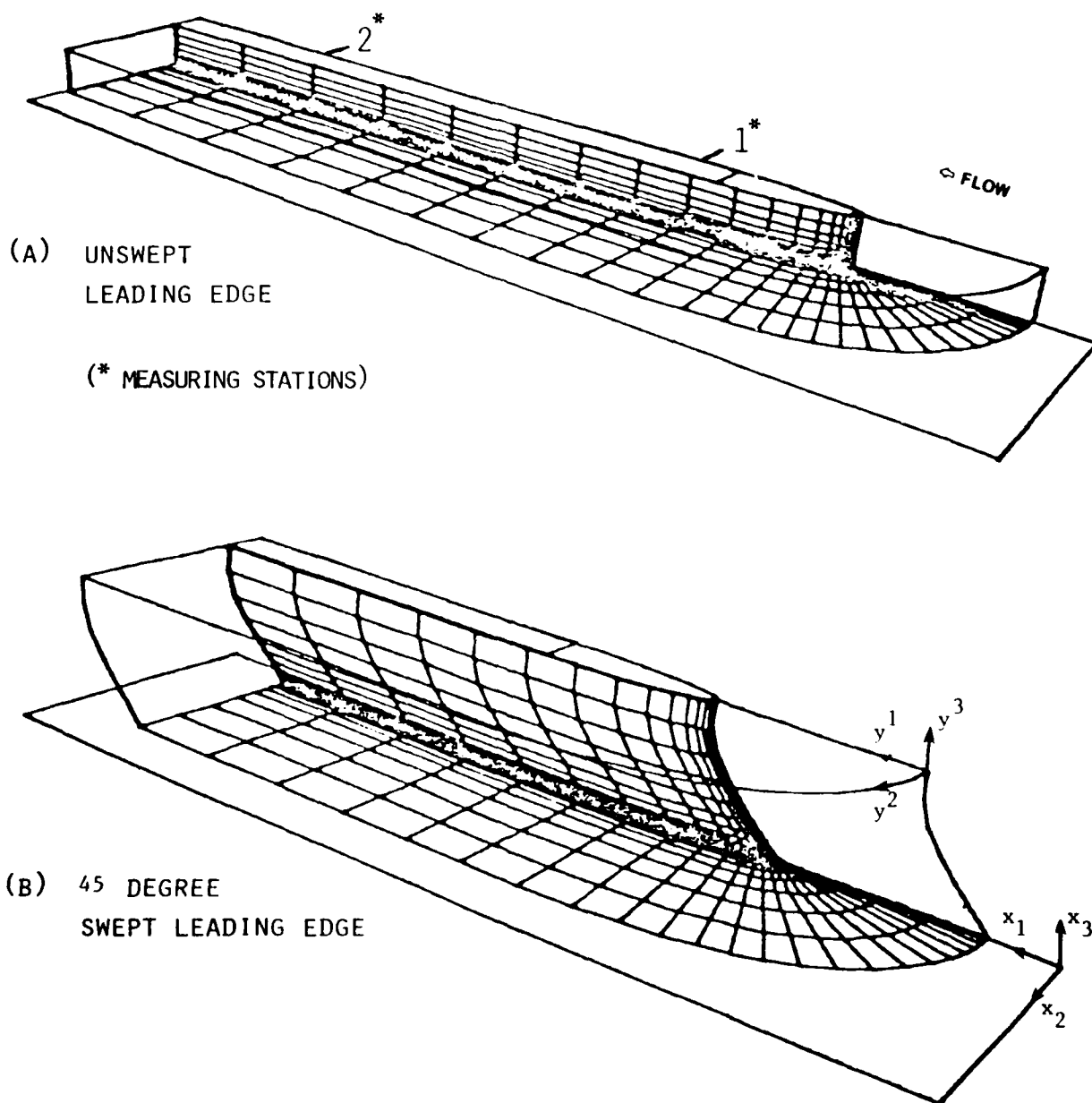
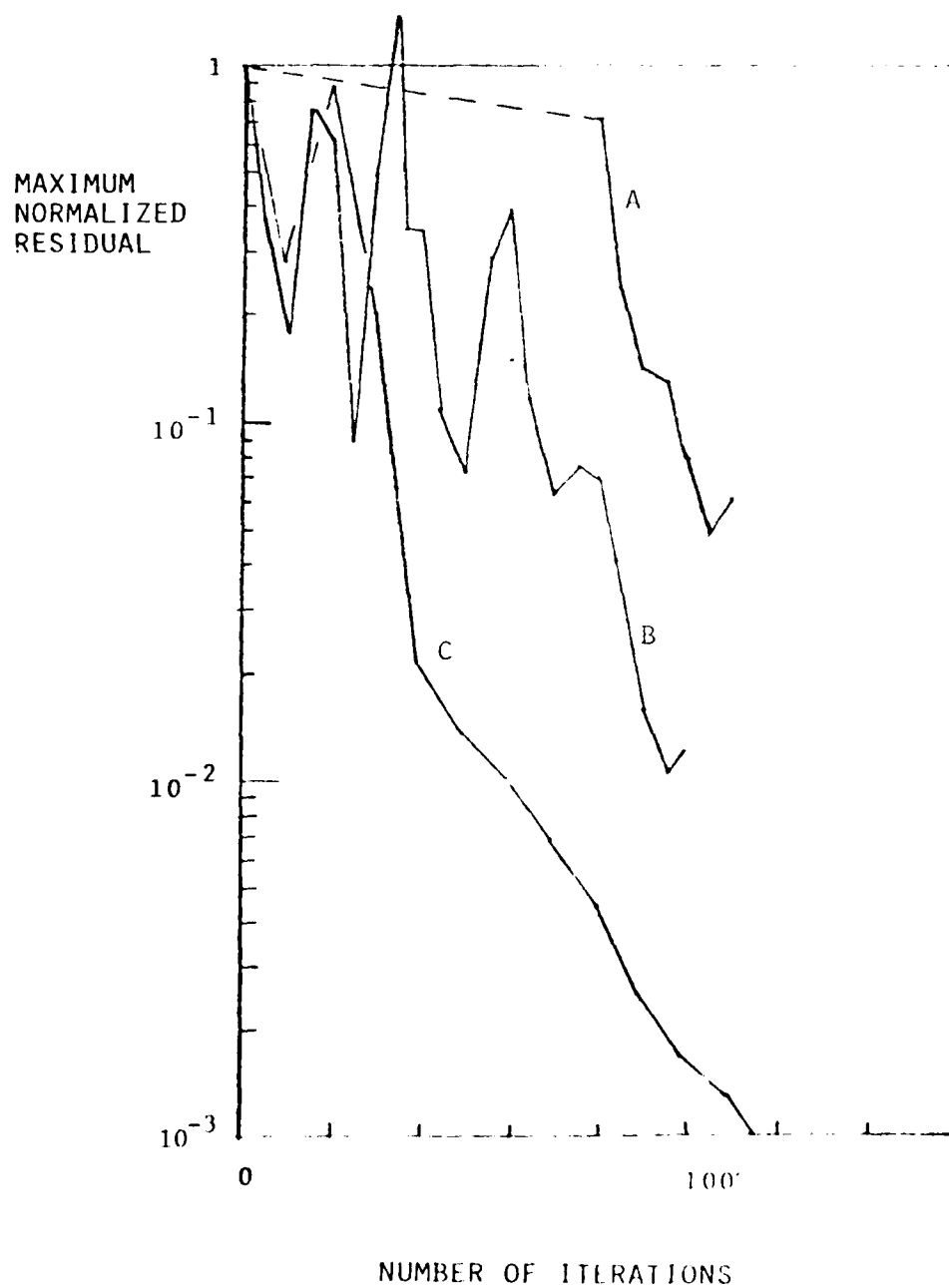


FIG. 2

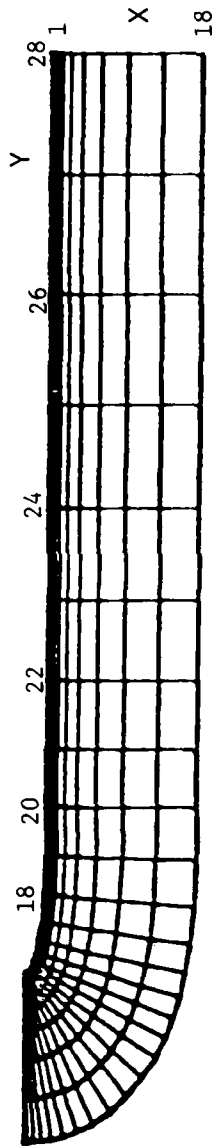
CONVERGENCE RATE FOR THREE-DIMENSIONAL TURBULENT LEADING-EDGE HORSESHOE VORTEX CALCULATION

- A - UNSWEPT LEADING EDGE
- B - SWEEPED LEADING EDGE
- C - TWO-DIMENSIONAL TURBULENT FLOW CASE



COORDINATES FOR TURBULENT LEADING EDGE HORSESHOE VORTEX FLOW

$Re = 132,000$ $M = 0.05$



COMPUTATIONAL REGION AND GRID

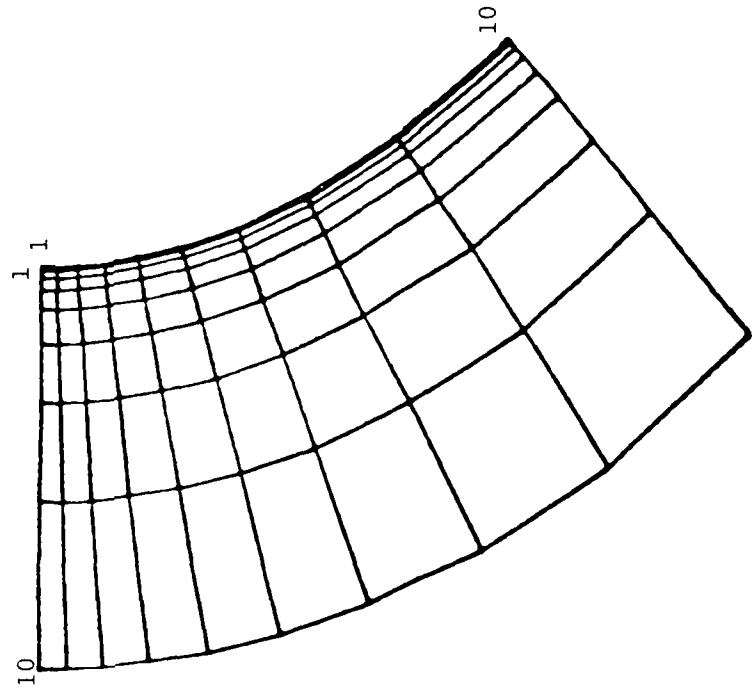
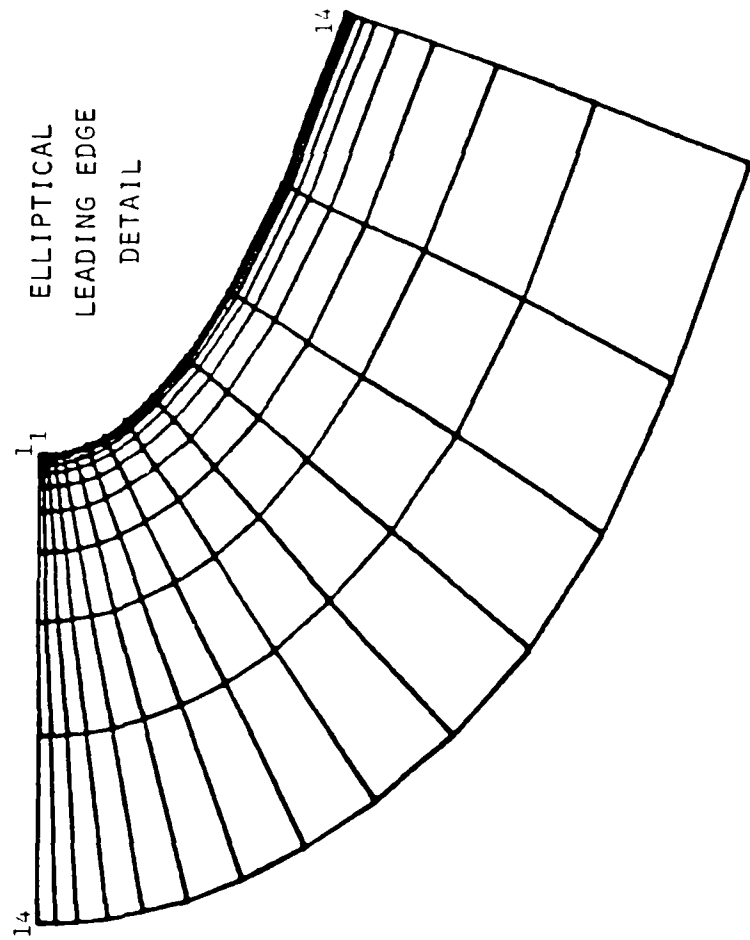
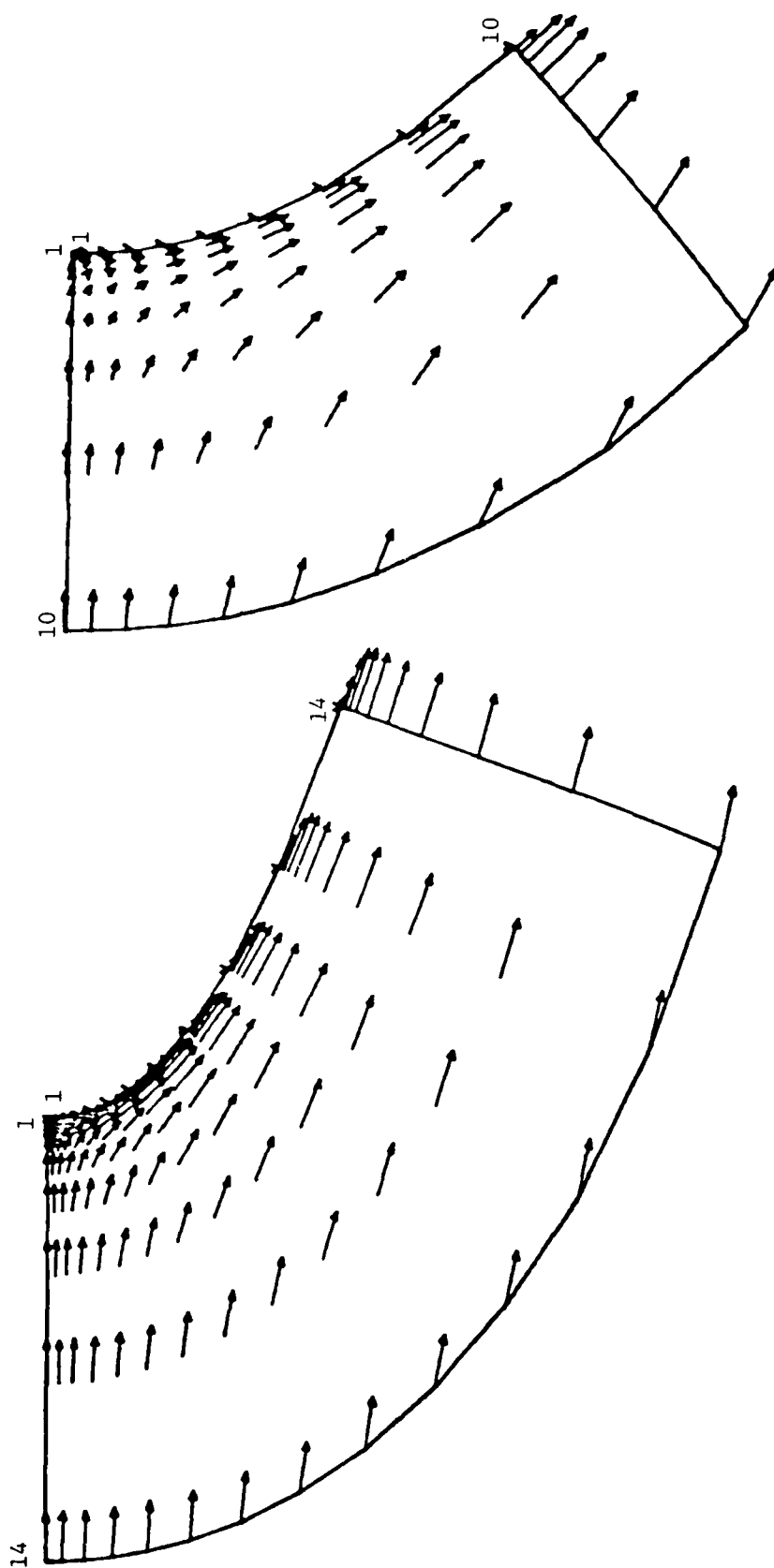


FIG. 3

FIG. 4

DETAIL OF FREE STREAM FLOW PATTERN
(TWO-DIMENSIONAL FLOW REGION AT SYMMETRY PLANE)



DETAIL OF ENDWALL FLOW PATTERN
(PLANE OF GRID POINTS ADJACENT TO WALL)

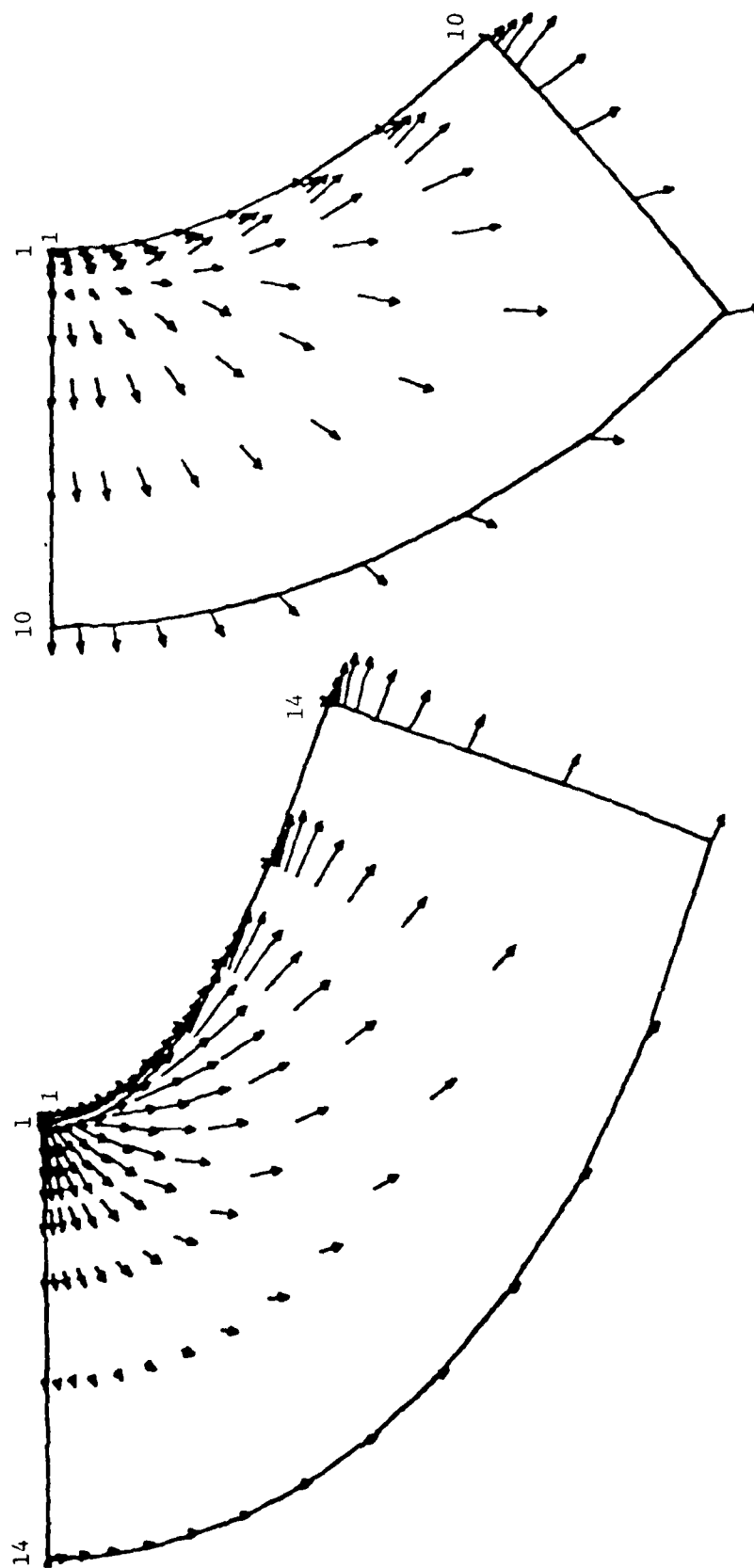
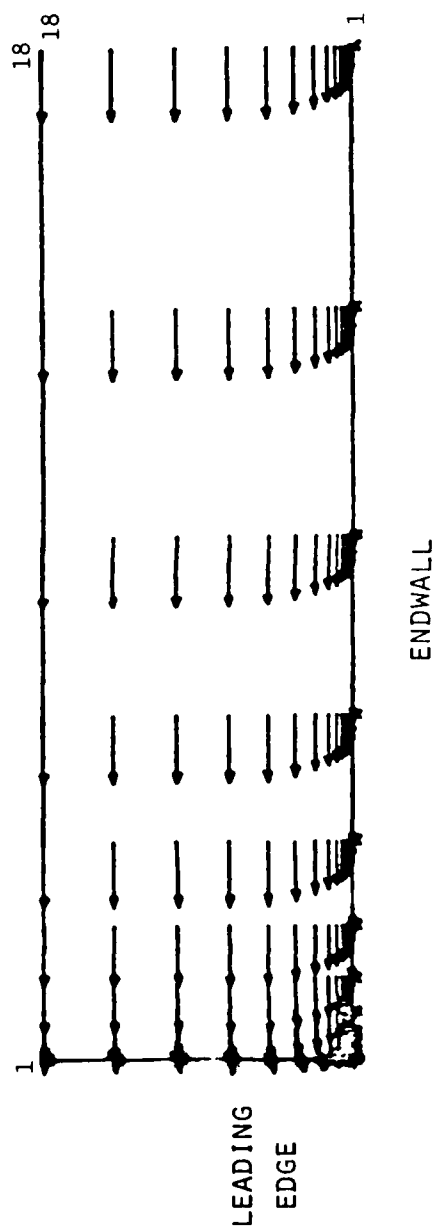
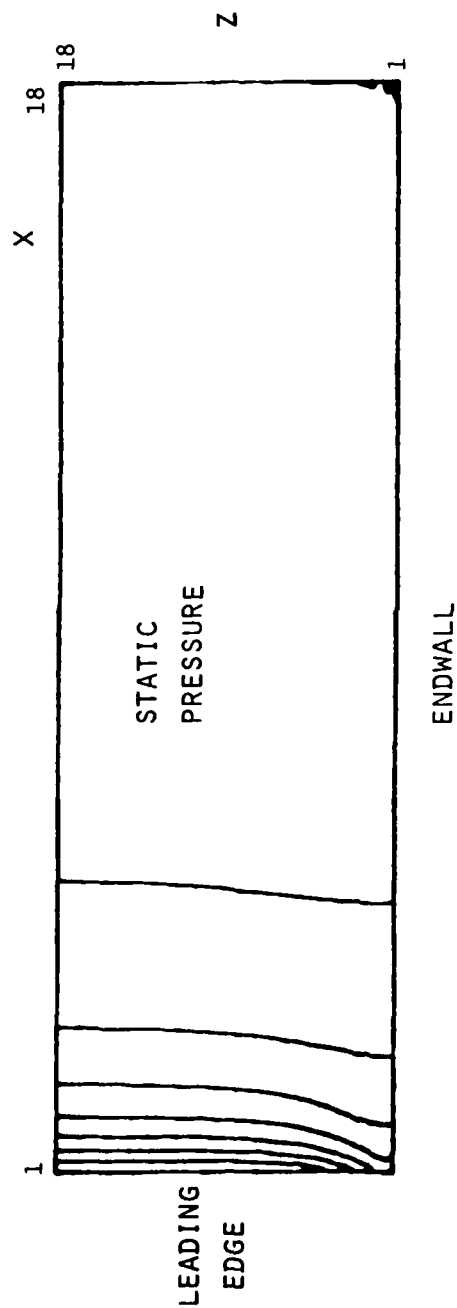


FIG. 5

FIG. 6

FLOW IN STAGNATION PLANE

(PLANE PARALLEL TO FREESTREAM FLOW
CONTAINING LEADING EDGE)



DETAIL OF HORSESHOE VORTEX FLOW IN STAGNATION PLANE

(NEAR INTERSECTION OF LEADING EDGE AND ENDWALL)

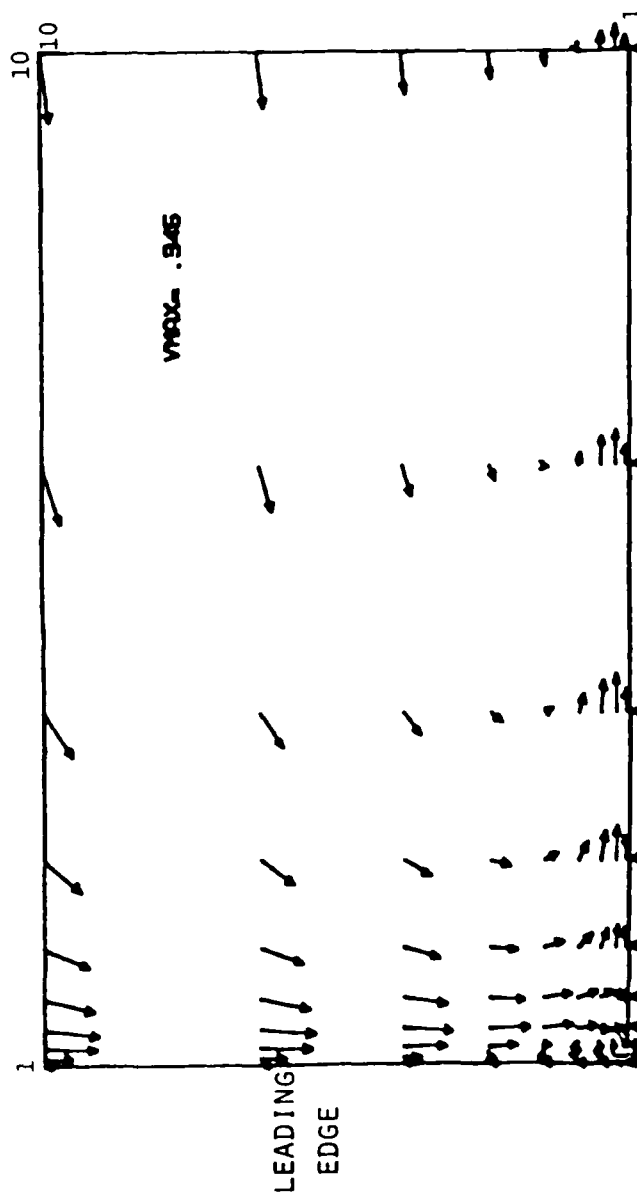
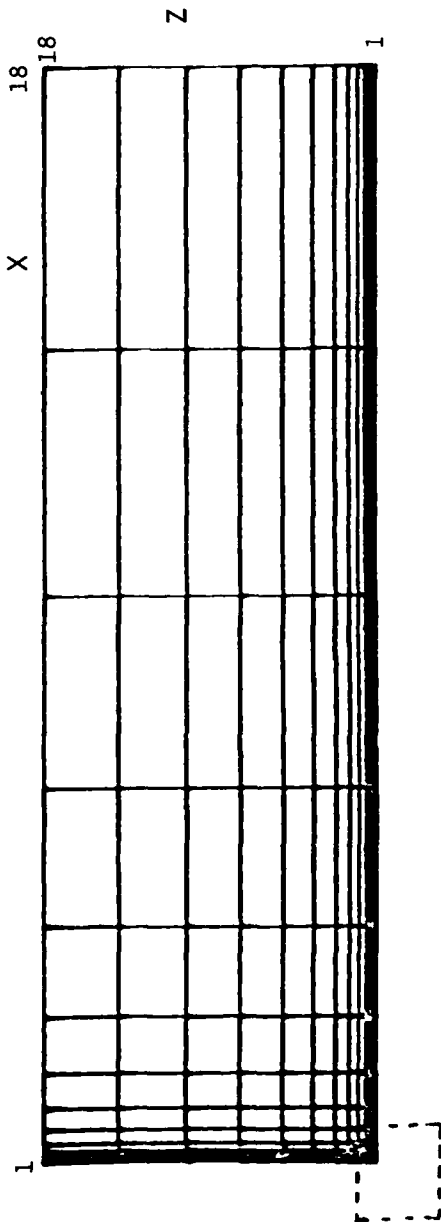


FIG. 7

FLOW AT THE END OF THE ELLIPTICAL LEADING EDGE REGION

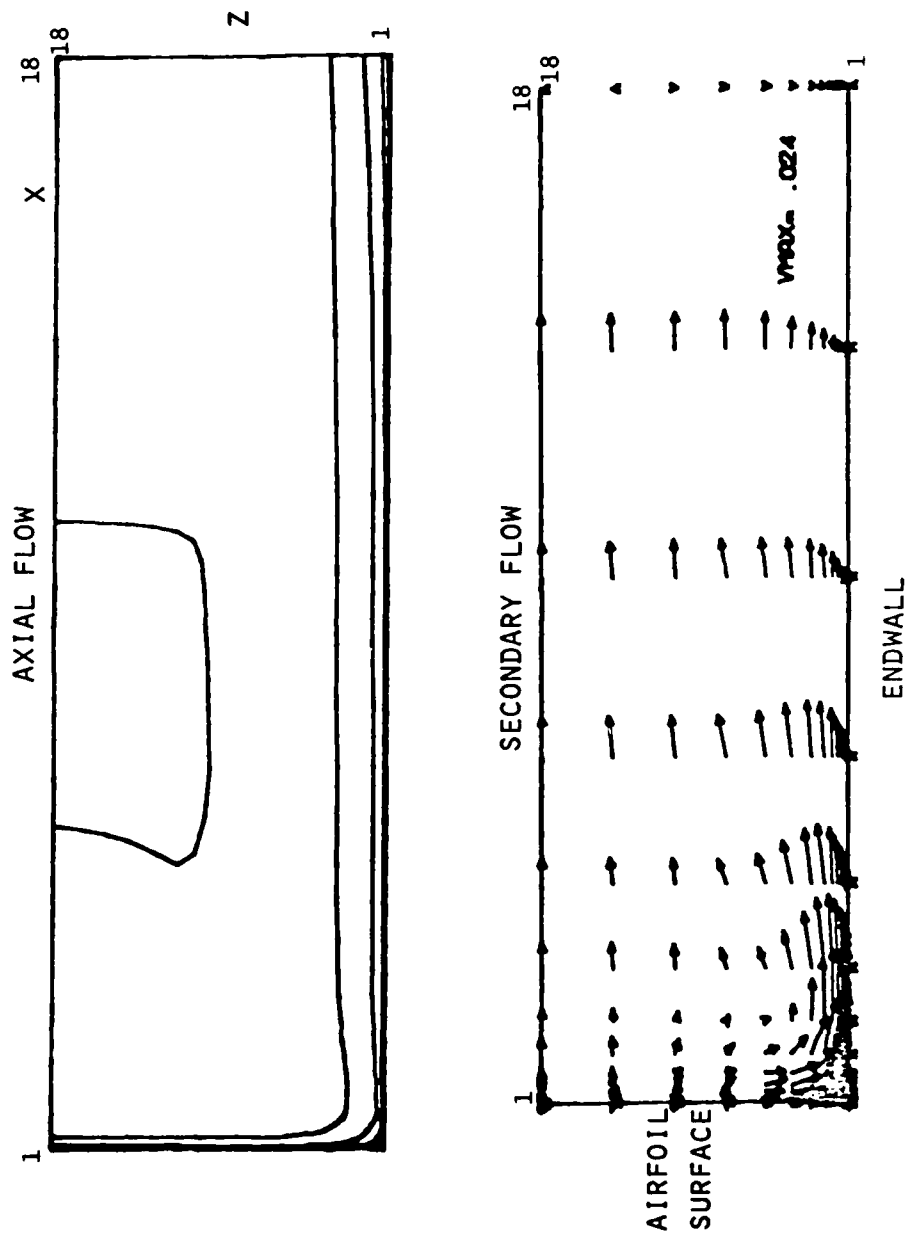
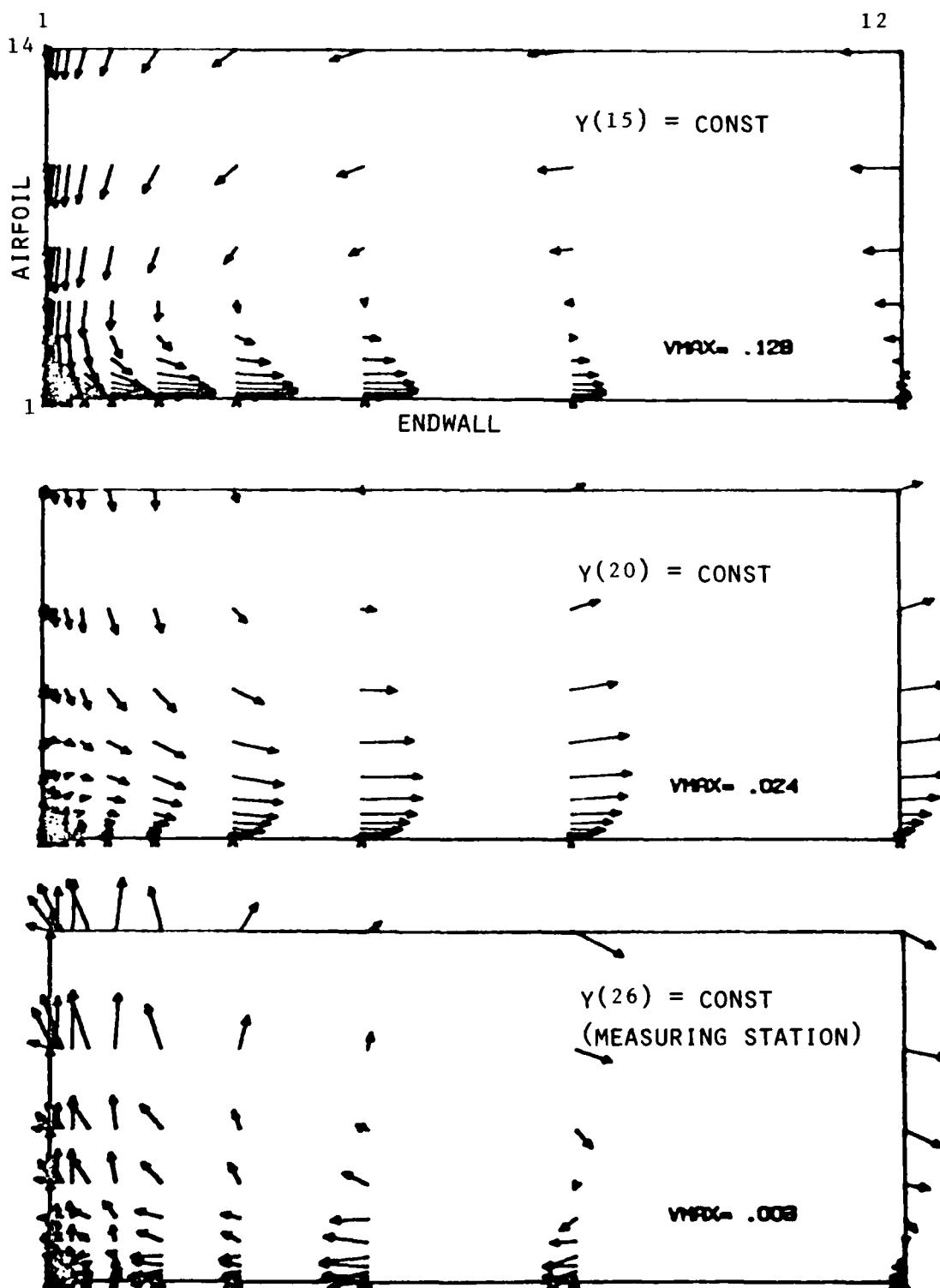


FIG. 8

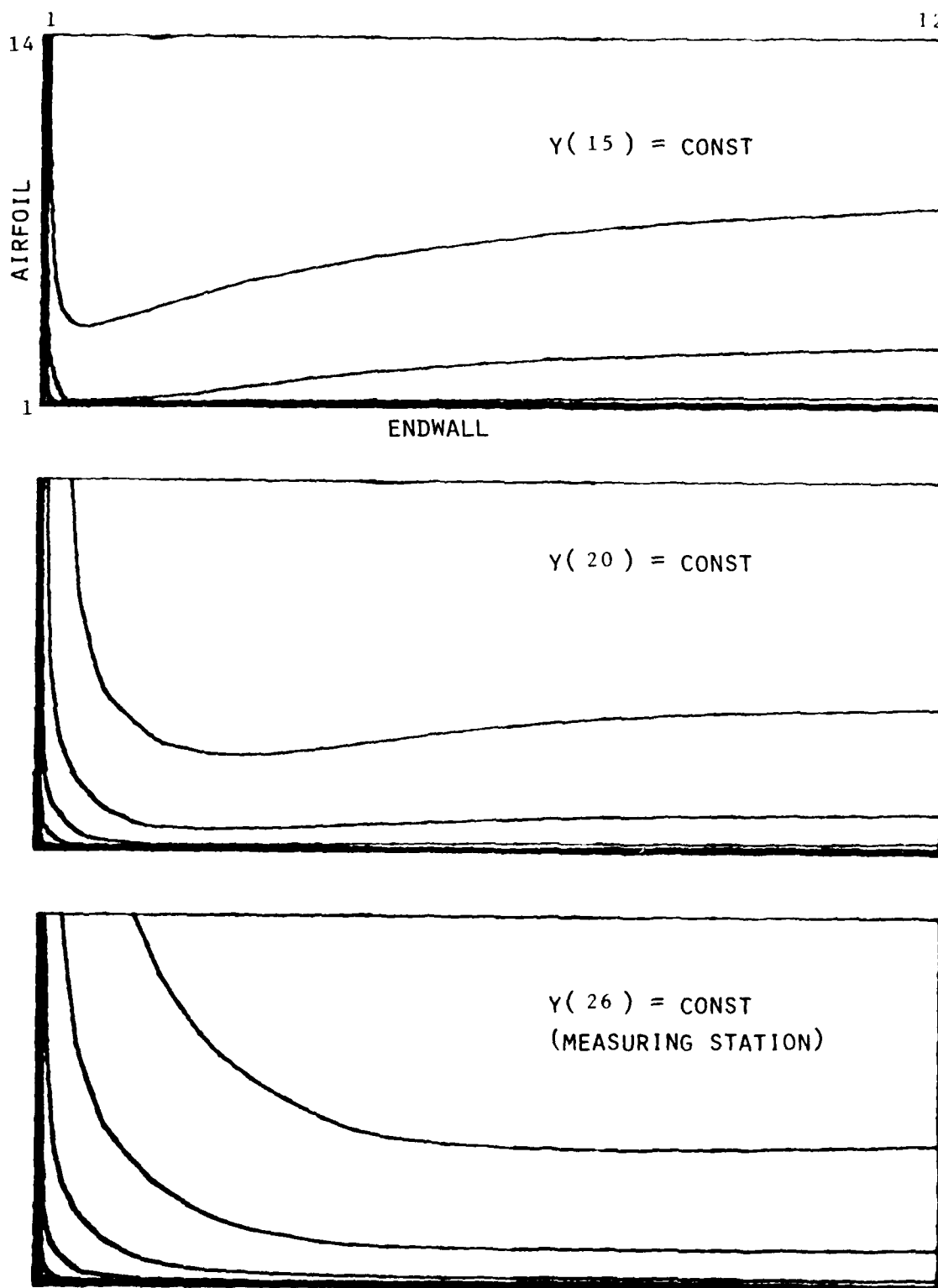
DETAIL OF CORNER FLOW DOWNSTREAM OF
UNSWEPT ELLIPTICAL LEADING EDGE
(TRANSVERSE VELOCITY)

FIG. 9



DETAIL OF CORNER FLOW DOWNSTREAM OF
UNSWEPT ELLIPTICAL LEADING EDGE
(CONTOURS OF AXIAL VELOCITY)

FIG. 10

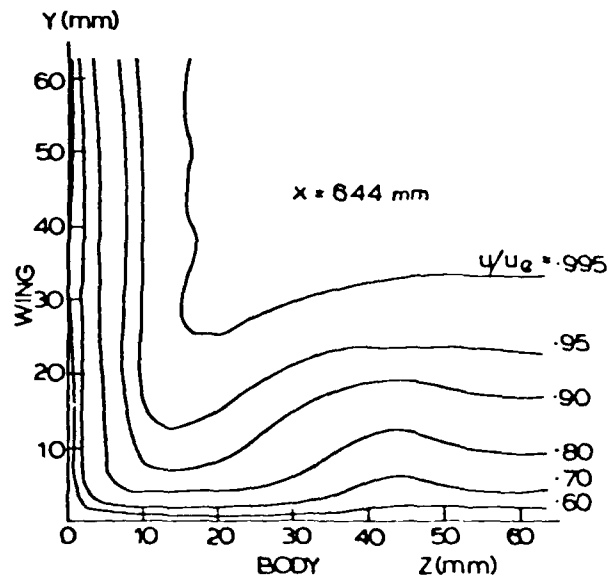


MEASUREMENTS OF SHABAKA AND BRADSHAW FOR
CORNER FLOW DOWNSTREAM OF UNSWEPT ELLIPTICAL
LEADING EDGE

FIG. 11

(APPROXIMATELY 4 HALF CHORDS DOWNSTREAM OF LEADING EDGE)

(A) AXIAL
VELOCITY



(B) TRANSVERSE
VELOCITY

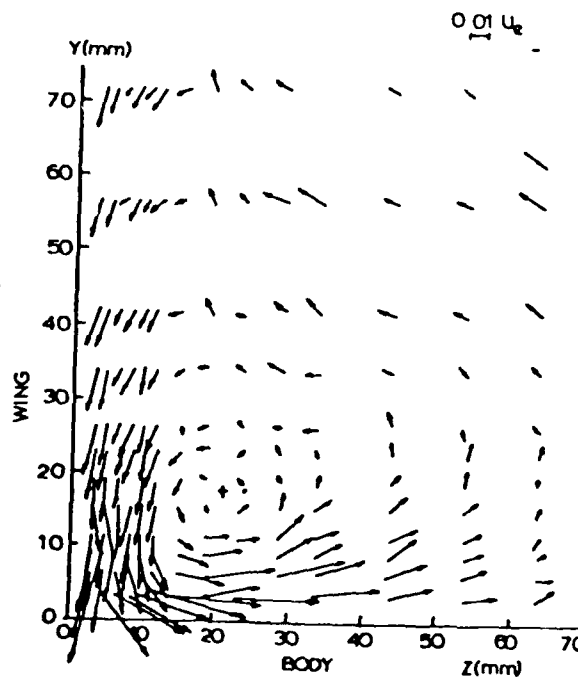


FIG. 12

GRID DISTRIBUTION

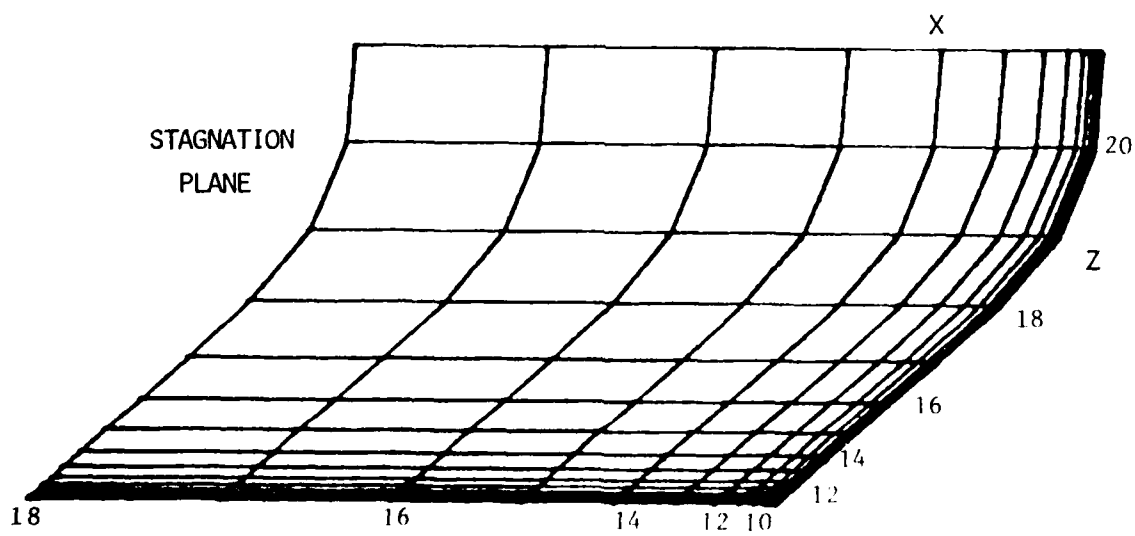
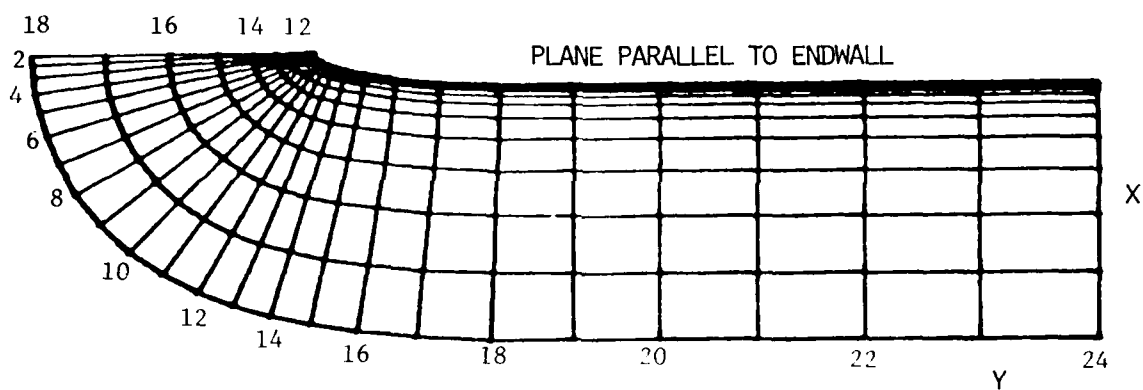
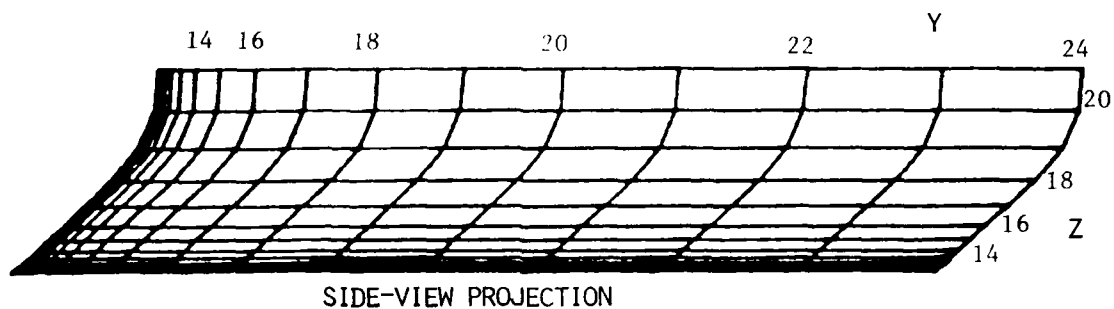
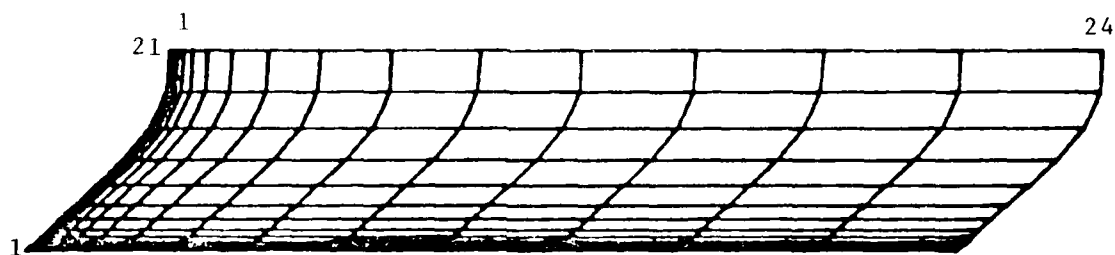
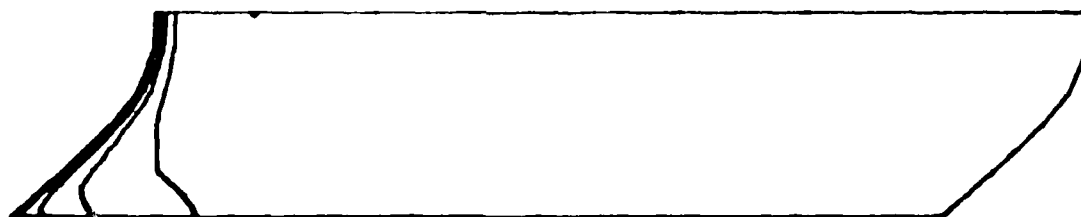


FIG. 13

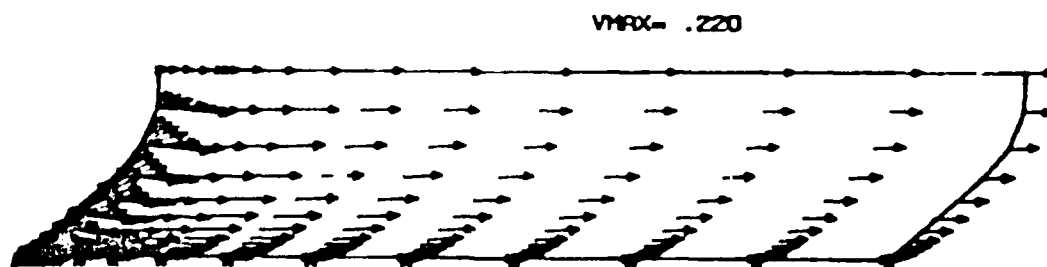
FLOW ADJACENT TO SURFACE OF AIRFOIL



(A) GRID



(B) PRESSURE



(C) VELOCITY
(SURFACE TUFT VISUALIZATION)

FIG. 14

DETAIL OF FLOW ADJACENT TO
SURFACE OF AIRFOIL

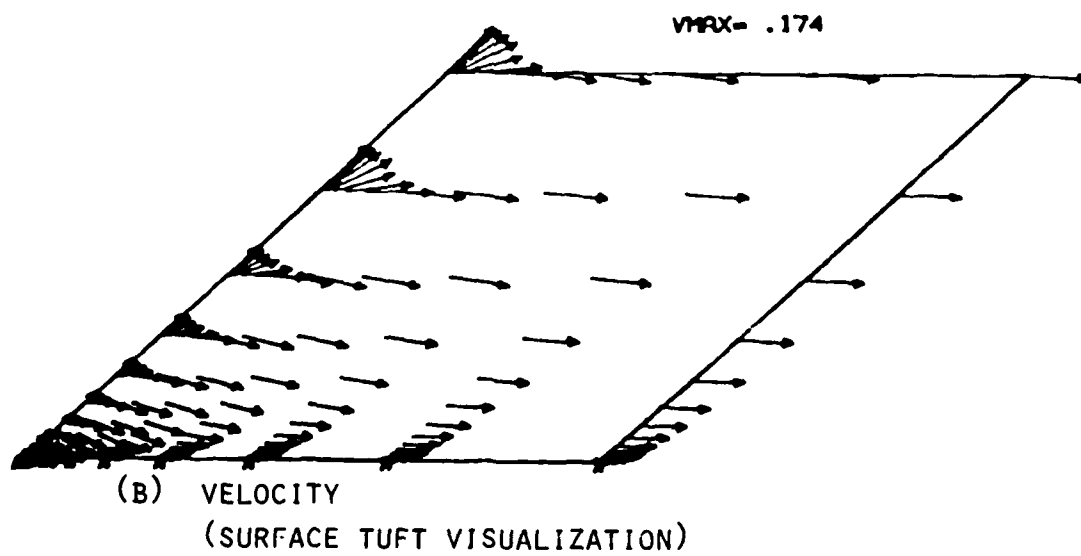
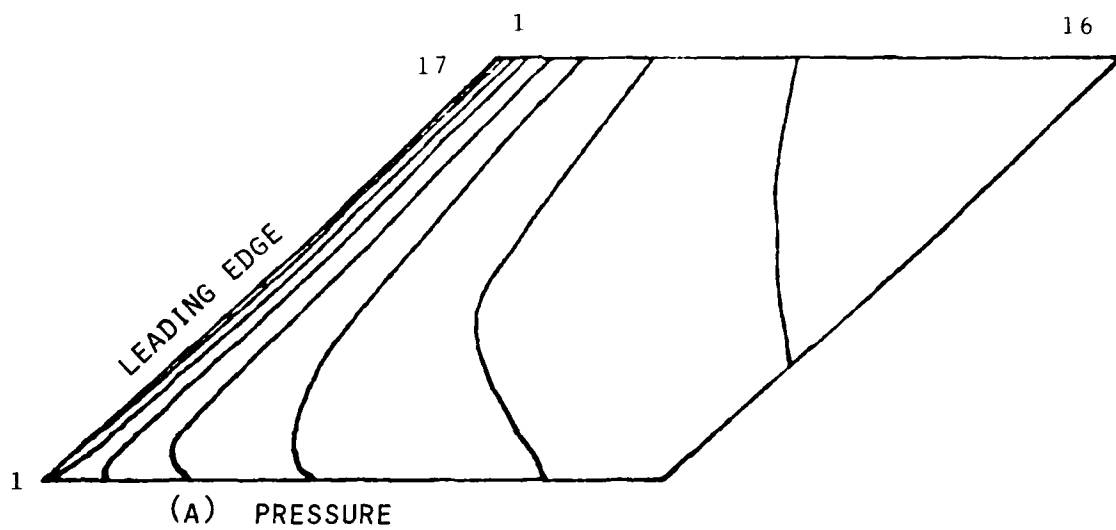
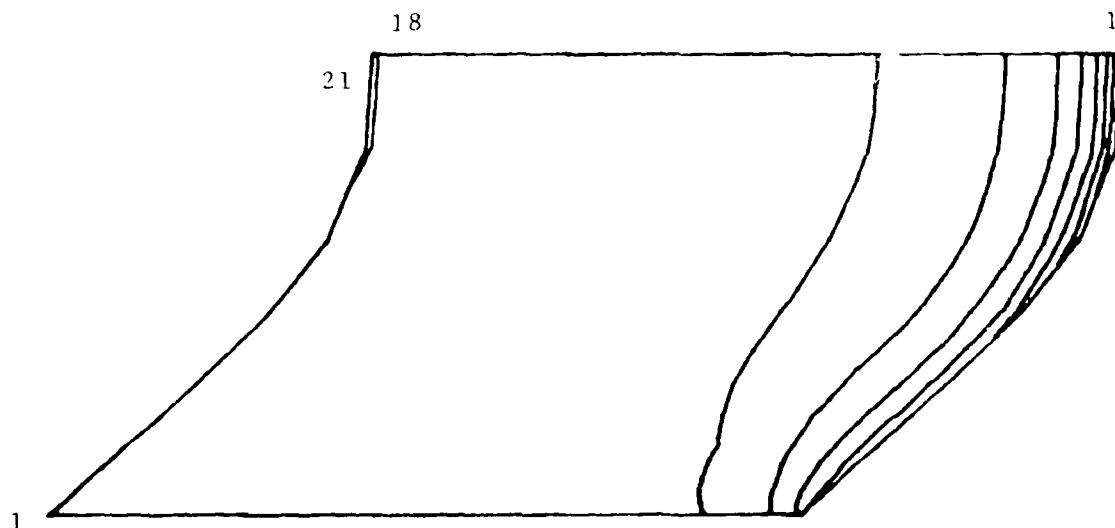
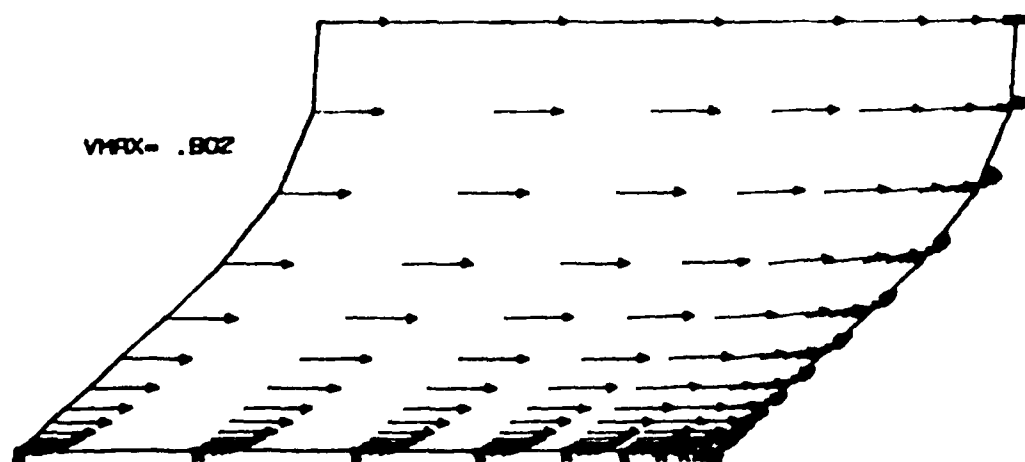


FIG. 15

FLOW IN STAGNATION PLANE UPSTREAM
OF LEADING EDGE



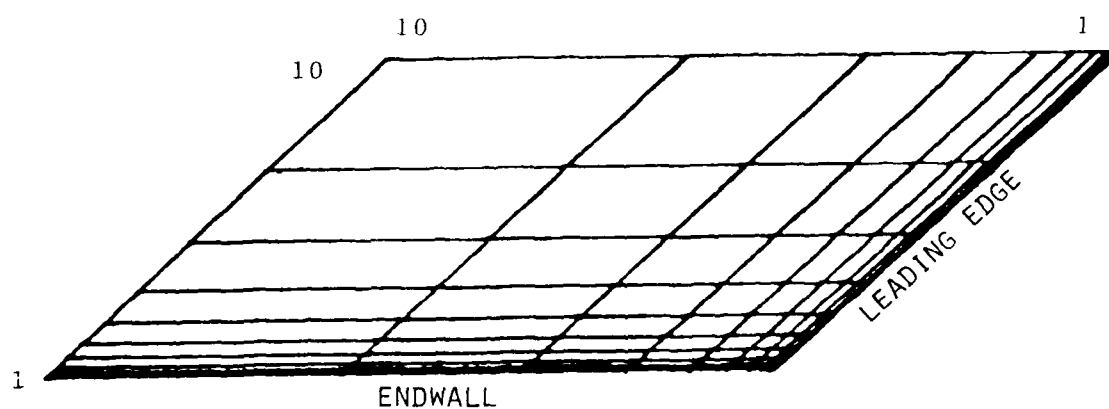
(A) PRESSURE



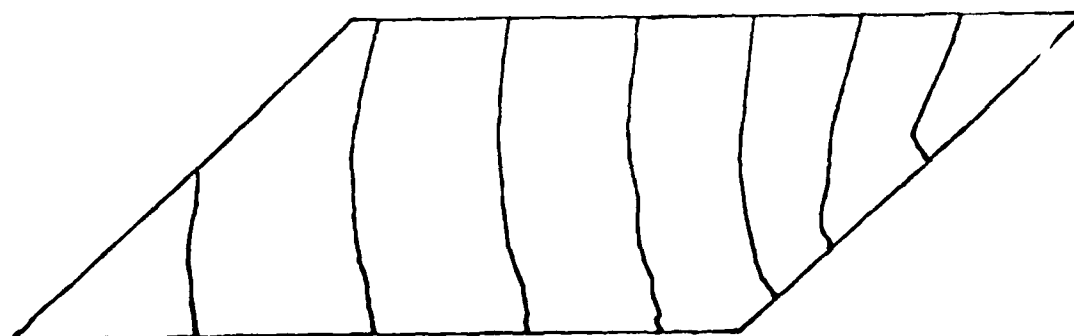
VHFX = .802

(B) VELOCITY

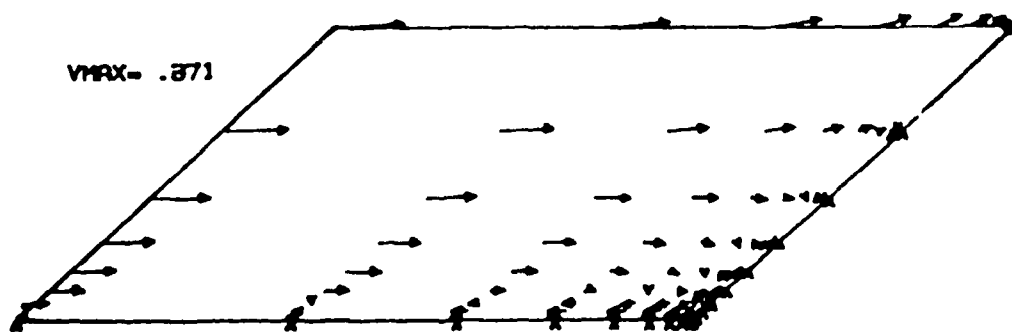
DETAIL OF FLOW IN STAGNATION PLANE
UPSTREAM OF LEADING EDGE



(A) GRID



(B) PRESSURE



(C) VELOCITY

FIG. 17

SOLUTION IN PLANE PARALLEL TO FLAT PLATE
($Z_{(16)} = \text{CONST}$)

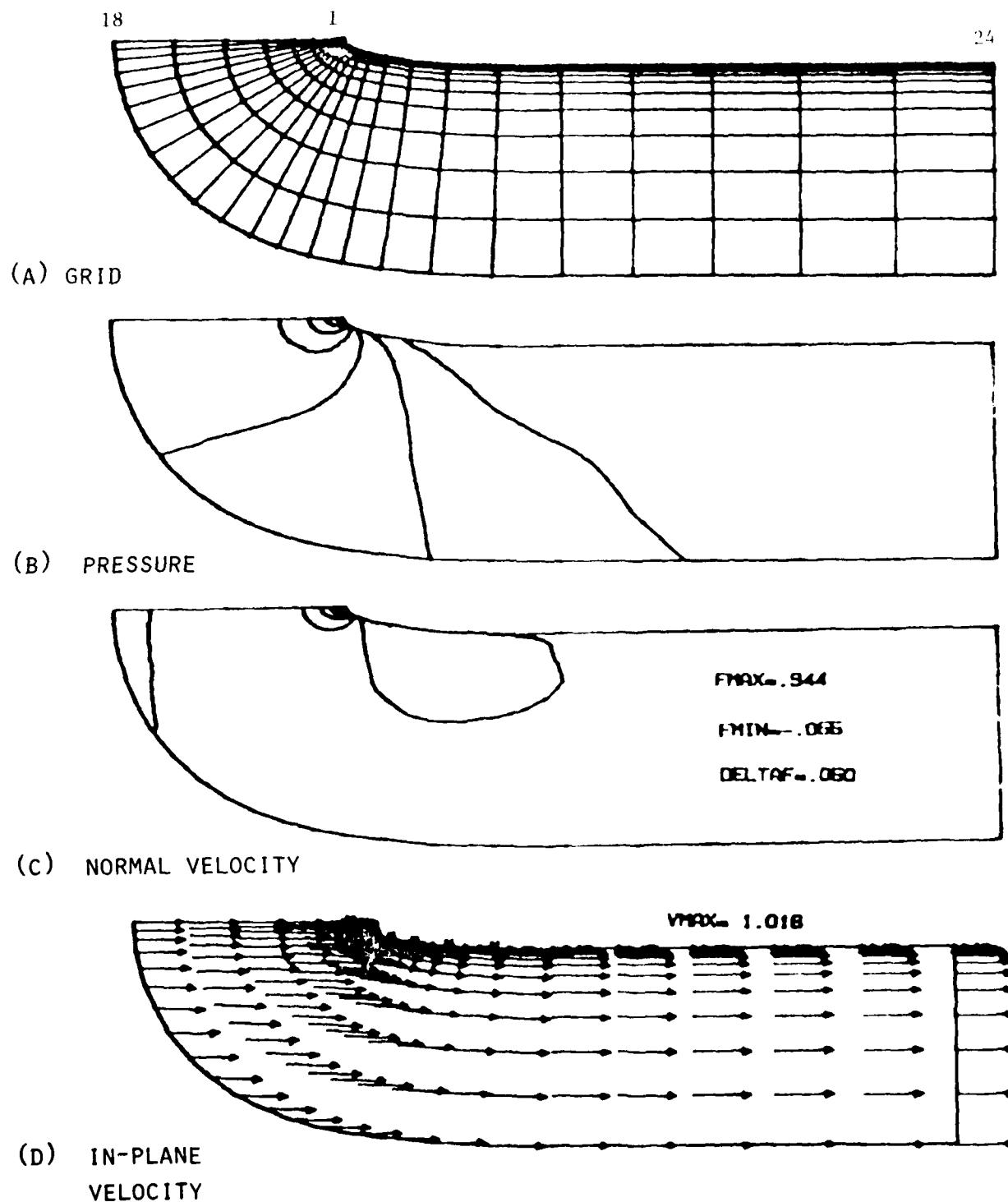
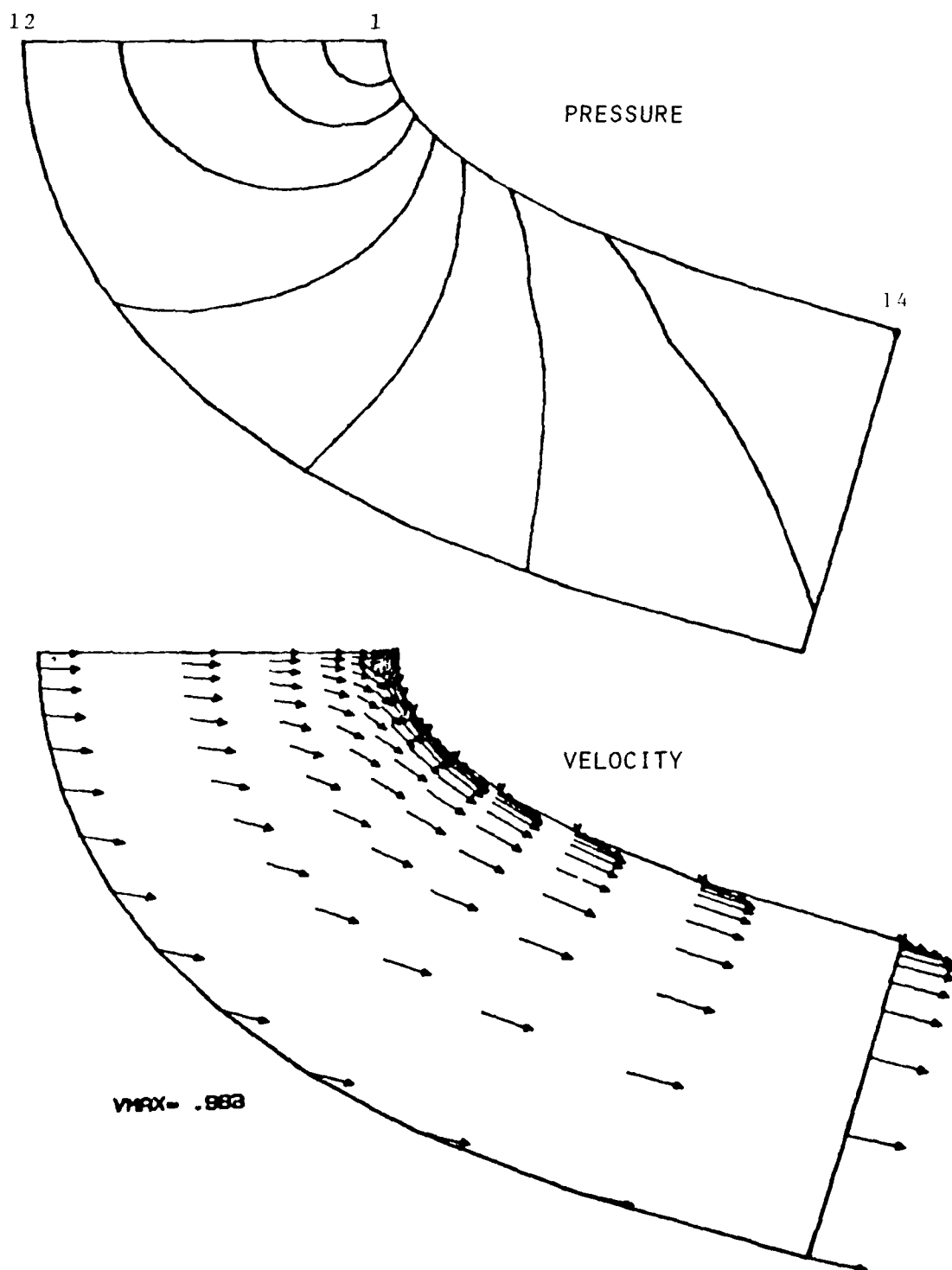
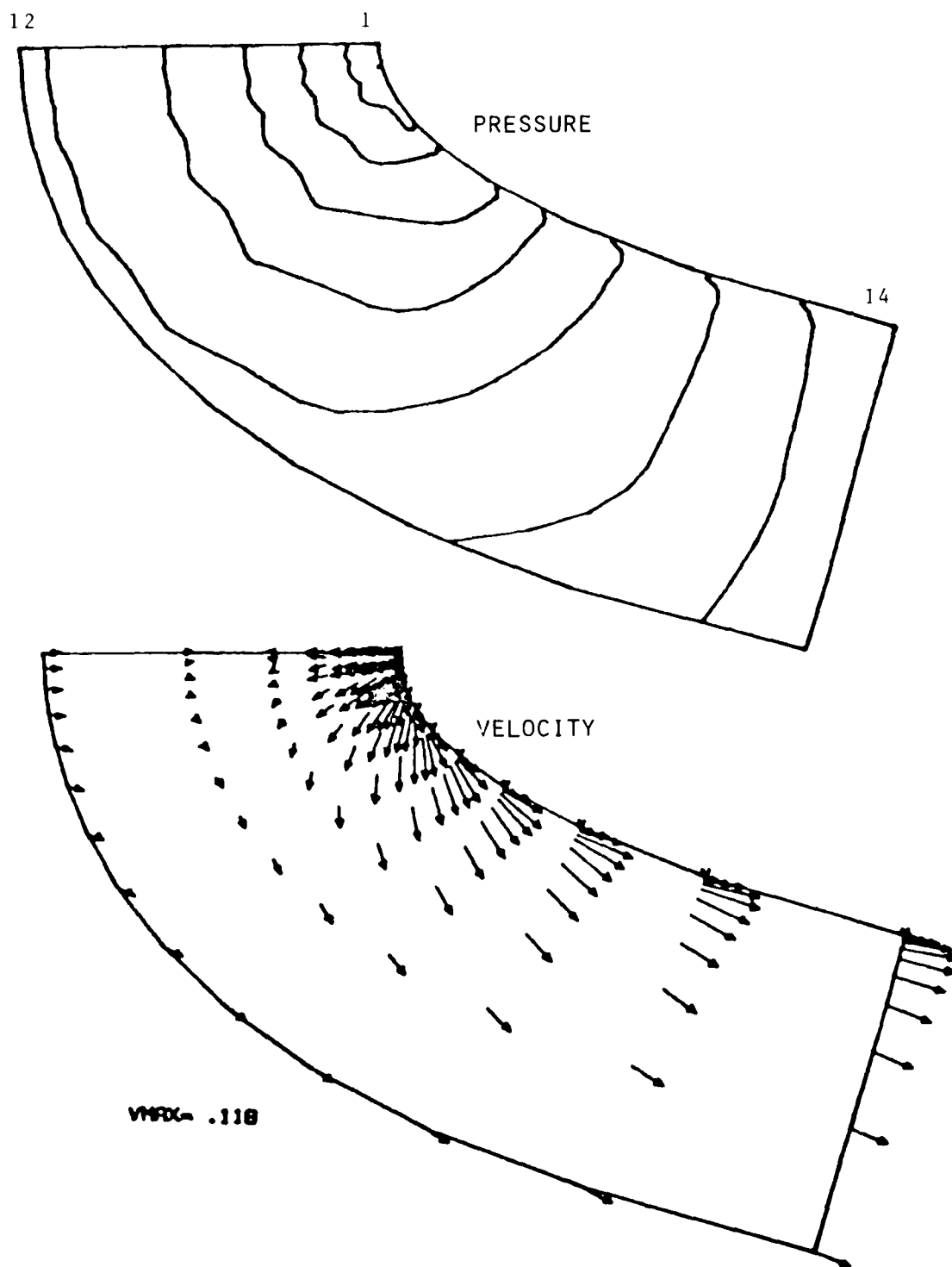


FIG. 18

DETAIL OF FREESTREAM FLOW PATTERN
(FREESTREAM SYMMETRY PLANE)



DETAIL OF ENDWALL FLOW PATTERN
(PLANE OF GRID POINTS ADJACENT TO ENDWALL)



DETAIL OF CORNER FLOW DOWNSTREAM
OF SWEEPED ELLIPTICAL LEADING EDGE
(TRANSVERSE VELOCITY)

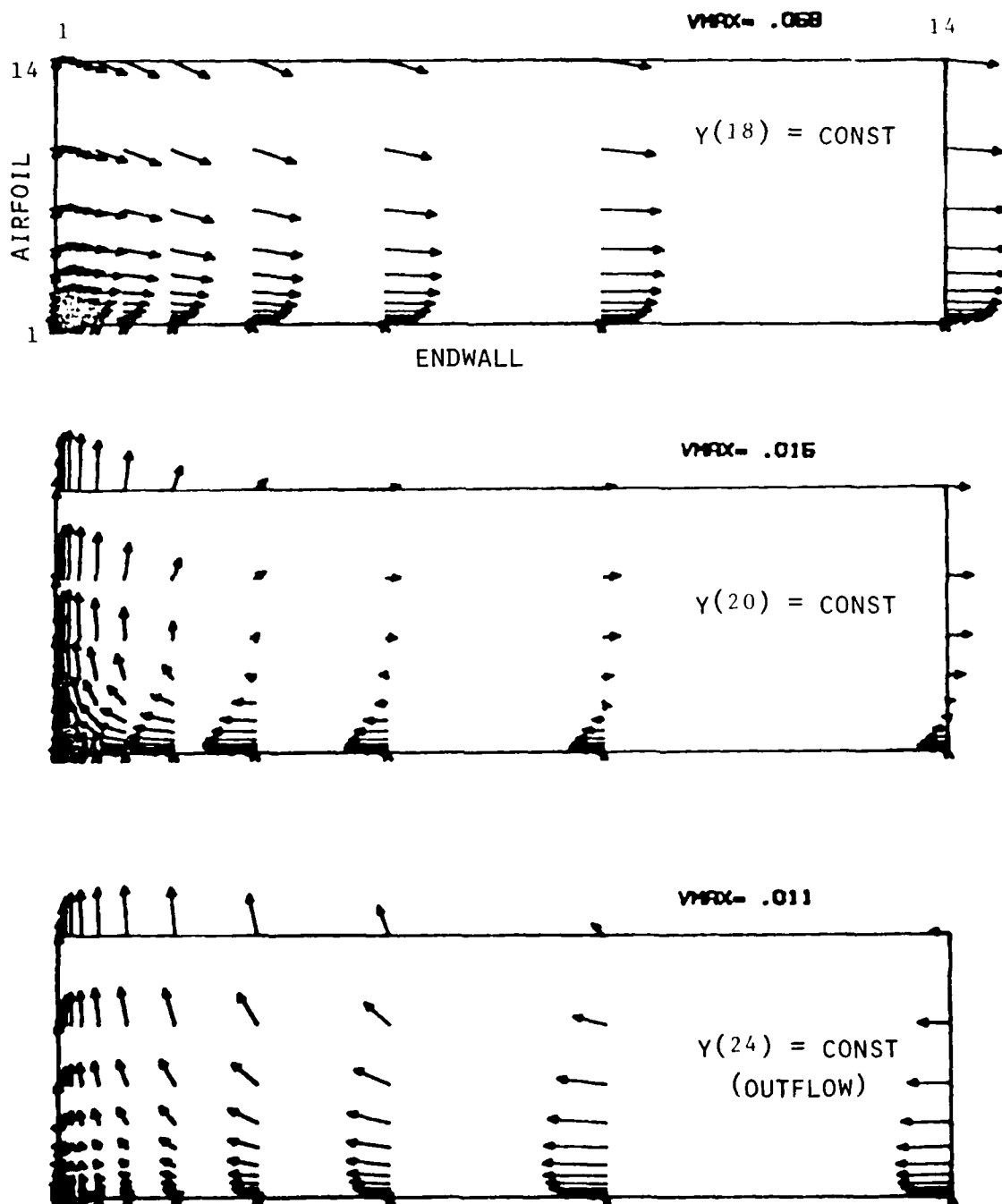
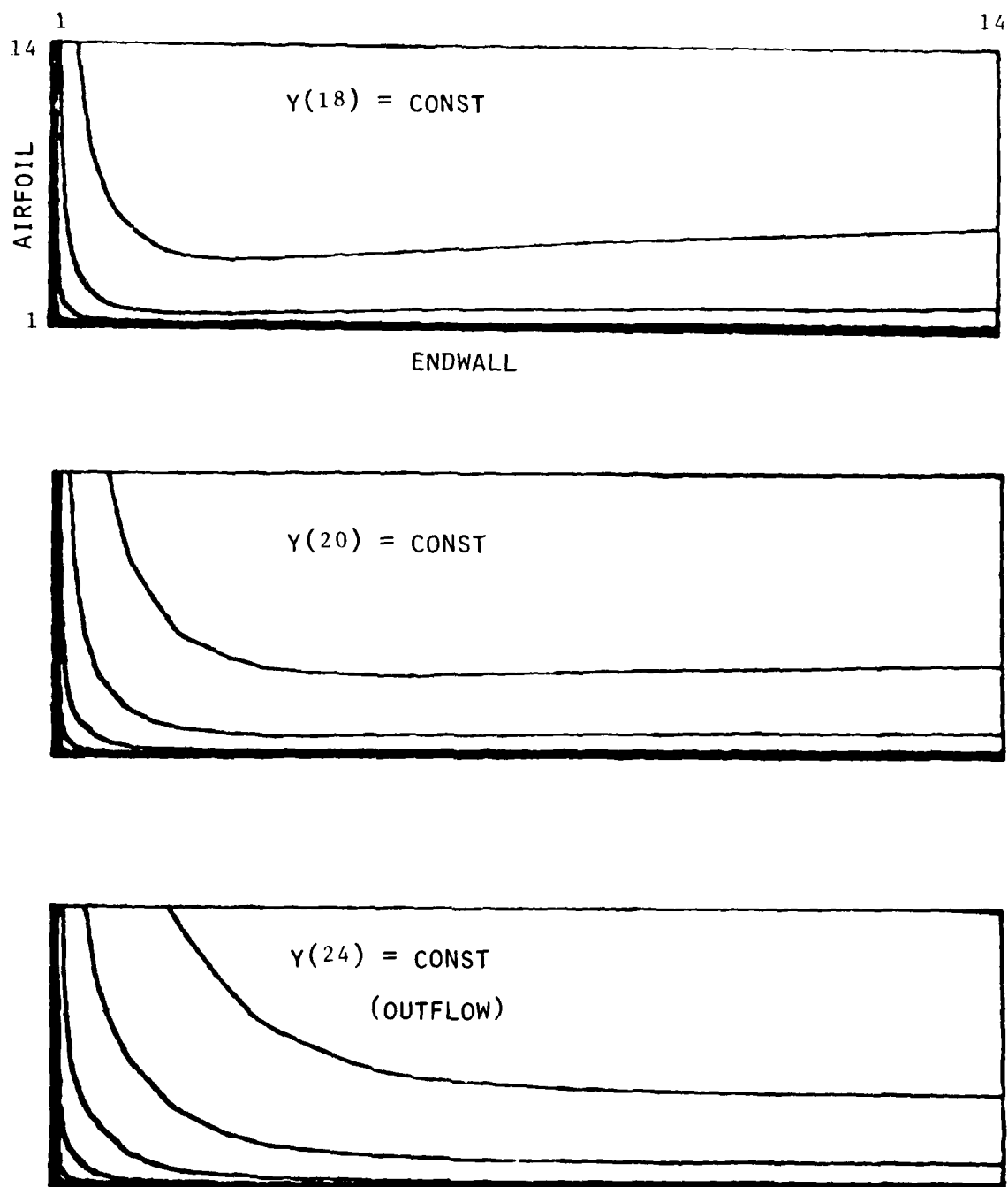


FIG. 21

DETAIL OF CORNER FLOW DOWNSTREAM
OF SWEEPED ELLIPTICAL LEADING EDGE
(CONTOURS OF AXIAL VELOCITY)



DISTRIBUTION LIST FOR UNCLASSIFIED
TECHNICAL REPORTS AND REPRINTS ISSUED UNDER
CONTRACT N00014-77-C-0075/TASK 061-245

All addresses receive one copy unless otherwise specified

Technical Library
Building 313
Ballistic Research Laboratories
Aberdeen Proving Ground, MD 21005

Mr. Aviars Celmins
Ballistic Research Laboratory
Ballistic Modelling Division
Aberdeen Proving Ground, MD 21005

Dr. P. J. Roache
Ecodynamics Research Associates, Inc.
P.O. Box 8172
Albuquerque, NM 87108

Defense Technical Information Center
Cameron Station
Building 5
Alexandria, VA 22314 12 copies

Library
Naval Academy
Annapolis, MD 21402

Director, Tactical Technology Office
Defense Advanced Research Projects Agency
1400 Wilson Boulevard
Arlington, VA 22209

Code 200B
Office of Naval Research
800 N. Quincy Street
Arlington, VA 22217

Code 438
Office of Naval Research
800 N. Quincy Street
Arlington, VA 22217 2 copies

Dr. J. L. Potter
Deputy Director, Technology
von Karman Gas Dynamics Facility
Arnold Air Force Station, TN 37389

Professor J. C. Wu
School of Aerospace Engineering
Georgia Institute of Technology
Atlanta, GA 30332

Library
Aerojet-General Corporation
6352 North Irwindale Avenue
Azusa, CA 91702

NASA Scientific and Technical
Information Facility
P.O. Box 8757
Baltimore/Washington International
Airport, MD 21240

Dr. K. C. Wang
College of Engineering
San Diego State University
San Diego, CA 92152

Professor A. J. Chorin
Department of Mathematics
University of California
Berkeley, CA 94720

Professor M. Holt
Department of Mechanical Engineering
University of California
Berkeley, CA 94720

Dr. H. R. Chaplin
Code 1600
David W. Taylor Naval Ship Research
and Development Center
Bethesda, MD 20084

Dr. Hans Lugt
Code 1802
David W. Taylor Naval Ship Research
and Development Center
Bethesda, MD 20084

Dr. Francois Frenkiel
Code 1802
David W. Taylor Naval Ship Research
and Development Center
Bethesda, MD 20084

DISTRIBUTION LIST (Continued)

Page 2

Dr. G. R. Inger
Department of Aerospace Engineering
Virginia Polytechnic Institute and
State University
Blacksburg, VA 24061

Professor C. H. Lewis
Department of Aerospace and Ocean Engineering
Virginia Polytechnic Institute and
State University
Blacksburg, VA 24061

Professor A. H. Nayfeh
Department of Engineering Science
Virginia Polytechnic Institute and
State University
Blacksburg, VA 24061

Dr. A. Rubel
Research Department
Grumman Aerospace Corporation
Bethpage, NY 11714

Director
Office of Naval Research Eastern/Central
Regional Office
666 Summer Street, Bldg. 114, Section D
Boston, MA 02210

Dr. J. C. Erickson, Jr.
CALSPAN Corporation
Advanced Technology Center
P.O. Box 400
Buffalo, NY 14225

Dr. T. J. Falk
CALSPAN Corporation
Advanced Technology Center
P.O. Box 400
Buffalo, NY 14225

Dr. C. Witliff
CALSPAN Corporation
Advanced Technology Center
P.O. Box 400
Buffalo, NY 14225

Professor R. F. Probst
Department of Mechanical Engineering
Massachusetts Institute of Technology
Cambridge, MA 02139

Commanding Officer
Office of Naval Research Branch Office
536 South Clark Street
Chicago, IL 60605

Code 753
Naval Weapons Center
China Lake, CA 93555

Mr. J. Marshall
Code 4063
Naval Weapons Center
China Lake, CA 93555

Professor R. T. Davis
Department of Aerospace Engineering
University of Cincinnati
Cincinnati, OH 45221

Professor S. G. Rubin
Department of Aerospace Engineering
and Applied Mechanics
University of Cincinnati
Cincinnati, OH 45221

Library MS 60-3
NASA Lewis Research Center
21000 Brookpark Road
Cleveland, OH 44135

Dr. J. D. Anderson, Jr.
Chairman, Department of Aerospace
Engineering
College of Engineering
University of Maryland
College Park, MD 20742

Professor O. Burggraf
Department of Aeronautical and
Astronautical Engineering
Ohio State University
1314 Kinnear Road
Columbus, OH 43212

Technical Library
Naval Surface Weapons Center
Dahlgren Laboratory
Dahlgren, VA 22448

Dr. F. Moore
Naval Surface Weapons Center
Dahlgren Laboratory
Dahlgren, VA 22448

Technical Library 2-51131
LTV Aerospace Corporation
P.O. Box 5907
Dallas, TX 75222

DISTRIBUTION LIST (Continued)
Page 3

Library, United Aircraft Corporation
Research Laboratories
Silver Lane
East Hartford, CT 06108

Professor G. Moretti
Polytechnic Institute of New York
Long Island Center
Department of Aerospace Engineering and
Applied Mechanics
Route 110
Framingdale, NY 11735

Dr. W. R. Briley
Scientific Research Associates, Inc.
P.O. Box 498
Glastonbury, CT 06033

Professor P. Gordon
Caluret Campus
Department of Mathematics
Purdue University
Hammond, IN 46323

Library (MS 185)
NASA-Langley Research Center
Langley Station
Hampton, VA 23665

Professor A. Chapmann
Chairman, Mechanical Engineering Department
William M. Rice Institute
Box 1892
Houston, TX 77001

Technical Library
Naval Ordnance Station
Indian Head, MD 20640

Professor D. A. Caughey
Sibley School of Mechanical and
Aerospace Engineering
Cornell University
Ithaca, NY 14850

Professor E. L. Resler
Sibley School of Mechanical and
Aerospace Engineering
Cornell University
Ithaca, NY 14850

Professor S. F. Shen
Sibley School of Mechanical and
Aerospace Engineering
Cornell University
Ithaca, NY 14850

Library
Midwest Research Institute
425 Volker Boulevard
Kansas City, MO 64110

Dr. M. M. Hafez
Flow Research, Inc.
P.O. Box 5040
Kent, WA 98031

Dr. E. M. Murman
Flow Research, Inc.
P.O. Box 5040
Kent, WA 98031

Dr. J. J. Riley
Flow Research, Inc.
P.O. Box 5040
Kent, WA 98031

Dr. S. A. Orszag
Cambridge Hydrodynamics, Inc.
54 Baskin Road
Lexington, MA 02173

Dr. P. Bradshaw
Imperial College of Science
and Technology
Department of Aeronautics
Prince Consort Road
London SW7 2BY, England

Professor T. Cebeci
Mechanical Engineering Department
California State University,
Long Beach
Long Beach, CA 90840

Dr. H. K. Cheng
University of Southern California
Department of Aerospace Engineering
University Park
Los Angeles, CA 90007

DISTRIBUTION LIST (Continued)

Page 4

Professor J. D. Cole
Mechanics and Structures Department
School of Engineering and Applied Science
University of California
Los Angeles, CA 90024

Engineering Library
University of Southern California
Box 77929
Los Angeles, CA 90007

Dr. C.-M. Ho
Department of Aerospace Engineering
University of Southern California
University Park
Los Angeles, CA 90007

Dr. T. D. Taylor
The Aerospace Corporation
P.O. Box 92957
Los Angeles, CA 90009

Commanding Officer
Naval Ordnance Station
Louisville, KY 40214

Mr. B. H. Little, Jr.
Lockheed-Georgia Company
Department 72-74, Zone 369
Marietta, GA 30061

Professor E. R. G. Eckert
University of Minnesota
241 Mechanical Engineering Building
Minneapolis, MN 55455

Dr. Gary Chapman
Mail Stop 227-4
Ames Research Center
Moffett Field, CA 94035

Library
Naval Postgraduate School
Monterey, CA 93940

Dr. J. L. Steger
Flow Simulations, Inc.
735 Alice Avenue
Mountain View, CA 94041

Dr. S. S. Stahara
Nielsen Engineering and Research, Inc.
410 Clyde Avenue
Mountain View, CA 94043

Engineering Societies Library
345 East 47th Street
New York, NY 10017

Professor A. Jameson
Courant Institute of Mathematical
Sciences
New York University
251 Mercer Street
New York, NY 10012

Professor G. Miller
Department of Applied Science
New York University
26-36 Stuyvesant Street
New York, NY 10003

Office of Naval Research
New York Area Office
715 Broadway - 5th Floor
New York, NY 10003

Dr. A. Vaglio-Laurin
Department of Applied Science
New York University
26-36 Stuyvesant Street
New York, NY 10003

Mr. D. Farmer
Naval Ocean Research and Development
Activity
Code 332
NSTL Station, MS 39522

Librarian, Aeronautical Library
National Research Council
Montreal Road
Ottawa 7, Canada

Lockheed Missiles and Space Company
Technical Information Center
3251 Hanover Street
Palo Alto, CA 94304

Director
Office of Naval Research
Western Regional Office
1030 East Green Street
Pasadena, CA 91106

Engineering Division
California Institute of Technology
Pasadena, CA 91109

DISTRIBUTION LIST (Continued)

Page 5

Library

Jet Propulsion Laboratory
4800 Oak Grove Drive
Pasadena, CA 91103

Professor H. Liepmann
Department of Aeronautics
California Institute of Technology
Pasadena, CA 91109

Mr. L. I. Chasen, MGR-MSD Lib.
General Electric Company
Missile and Space Division
P.O. Box 8555
Philadelphia, PA 19101

Technical Library
Naval Missile Center
Point Mugu, CA 93042

Professor S. Bogdonoff
Gas Dynamics Laboratory
Department of Aerospace and
Mechanical Sciences
Princeton University
Princeton, NJ 08540

Professor S. I. Cheng
Department of Aerospace and
Mechanical Sciences
Princeton University
Princeton, NJ 08540

Dr. J. E. Yates
Aeronautical Research Associates
of Princeton, Inc.
50 Washington Road
Princeton, NJ 08540

Professor L. Sirovich
Division of Applied Mathematics
Brown University
Providence, RI 02912

Redstone Scientific Information Center
Chief, Document Section
Army Missile Command
Redstone Arsenal, AL 35809

U.S. Army Research Office
P.O. Box 12211
Research Triangle, NC 27709

Editor, Applied Mechanics Review
Southwest Research Institute
8500 Culebra Road
San Antonio, TX 78228

Library and Information Services
General Dynamics - CONVAIR
P.O. Box 1128
San Diego, CA 92112

Dr. R. Magnus
General Dynamics - CONVAIR
Kearny Mesa Plant
P.O. Box 80847
San Diego, CA 92138

Office of Naval Research
San Francisco Area Office
One Hallidie Plaza, Suite 601
San Francisco, CA 94102

Library
The RAND Corporation
1700 Main Street
Santa Monica, CA 90401

Dr. P. E. Rubbert
Boeing Aerospace Company
P.O. Box 3999
Mail Stop 41-18
Seattle, WA 98124

Librarian
Naval Surface Weapons Center
White Oak Laboratory
Silver Spring, MD 20910

Dr. J. M. Solomon
Naval Surface Weapons Center
White Oak Laboratory
Silver Spring, MD 20910

Professor J. H. Ferziger
Department of Mechanical Engineering
Stanford University
Stanford, CA 94305

Dr. H. Yoshihara
Boeing Aerospace Company
P.O. Box 3999
Mail Stop 41-18
Seattle, WA 98124

DISTRIBUTION LIST (Continued)

Page 6

Professor K. Karamcheti
Department of Aeronautics and
Astronautics
Stanford University
Stanford, CA 94305

Professor O. Bunemann
Institute for Plasma Research
Stanford University
Stanford, CA 94305

Engineering Library
McDonnell Douglas Corporation
Department 218, Building 101
P.O. Box 516
St. Louis, MO 63166

Dr. R. J. Hakkinen
McDonnell Douglas Corporation
Department 222
P.O. Box 516
St. Louis, MO 63166

Dr. N. Malmuth
Rockwell International Science Center
1049 Camino Dos Rios
P.O. Box 1085
Thousand Oaks, CA 91360

Library
Institute of Aerospace Studies
University of Toronto
Toronto 5, Canada

Professor W. R. Sears
Aerospace and Mechanical Engineering
University of Arizona
Tucson, AZ 85721

Professor A. R. Seebass
Department of Aerospace and
Mechanical Engineering
University of Arizona
Tucson, AZ 85721

Dr. K. T. Yen
Code 3015
Naval Air Development Center
Warminster, PA 18974

Air Force Office of Scientific
Research (SREM)
Building 1410, Bolling AFB
Washington, DC 20332

Chief of Research and Development
Office of Chief of Staff
Department of the Army
Washington, DC 20310

Library of Congress
Science and Technology Division
Washington, DC 20540

Director of Research (Code RR)
National Aeronautics and Space
Administration
600 Independence Avenue, SW
Washington, DC 20546

Library
National Bureau of Standards
Washington, DC 20234

National Science Foundation
Engineering Division
1800 G Street, NW
Washington, DC 20550

AIR 320D
Naval Air Systems Command
Washington, DC 20361

AIR 950D
Naval Air Systems Command
Washington, DC 20375

Code 2627
Naval Research Laboratory
Washington, DC 20375

SEA 03512
Naval Sea Systems Command
Washington, DC 20362

SEA 09G3
Naval Sea Systems Command
Washington, DC 20362

Dr. Charles Watkins, Head
Mechanical Engineering Department
Howard University
Washington, DC 20059

DISTRIBUTION LIST (Continued)

Page 7

Dr. A. L. Slafkosky
Scientific Advisor
Commandant of the Marine Corps
(Code AX)
Washington, DC 20380

Director
Weapons Systems Evaluation Group
Washington, DC 20350

Research Library
AVCO Corporation
Missile Systems Division
201 Lovell Street
Wilmington, MA 01887

AFAPL (APRC)
AB
Wright Patterson, AFB, OH 45433

Dr. Donald J. Harney
AFFDL/FX
Wright Patterson, AFB, OH 45433

Dr. D. R. Kotansky
Department 341
P.O. Box 516
St. Louis, MO 63166

DATE
FILMED

105-18